Molecular dynamics simulations of ultrathin PMMA films

Lili Zhang[1] and Norman A. Fleck

Cambridge University, Engineering Department, Trumpington Street, Cambridge, CB2 1PZ, UK

Corresponding authors: lz399@cam.ac.uk (L. Zhang) and naf1@cam.ac.uk (N.A. Fleck)

Abstract

The mechanical properties of an ultrathin film made from a thermoplastic differ from the bulk due to the presence of the free surface. Here, molecular dynamics simulations are used to explore the thickness dependence of uniaxial and equi-biaxial tensile responses of polymethyl methacrylate (PMMA) films. The sensitivity of deformation response to temperature, molecular weight and the degree of side-branching is determined. We find that the tensile failure strain decreases with decreasing film thickness, temperature, and with decreasing molecular weight. The degree of side-branching plays a secondary role in dictating the tensile response. Failure is by the initiation of voids at the free surface, followed by the expansion of the voids in the thickness direction. Recent solid−state nanofoaming experiments and models suggest that the attainable porosity of nanofoams is less than that of macro−scale foams due to the reduced ductility of the cell walls of the nanofoam. Our results provide a physical explanation for this observation.

Keywords: Polymer film, PMMA, Nanofoaming, Failure strain, Molecular dynamics simulations

1. Introduction

In the bulk state, linear polymer melts are commonly modeled as ideal Gaussian chains. Each polymer chain has the form of a random walk with a length scale that is dependent on the molecular weight M_w of the polymer [1]. This characteristic length scale of a linear polymer chain can be described by the root−mean−square, end−to−end distance d_{ee}, where

[1]Current affiliation: Aarhus University, Department of Mechanical and Production Engineering, Inge Lehmanns Gade 10, 8000 Aarhus C, Denmark

$d_{ee} \sim {M_w}^{1/2}$. Due to random thermal motion, a polymer chain explores and occupies a pervaded volume V_p, where $V_p \sim d_{ee}^3$. Within V_p, the chain interacts with itself and with neighbouring chains. Some of these interactions restrict the mobility of the polymer chain, resulting in entanglements with other chains. These entanglements play a major role in dictating the mechanical properties of the bulk polymer [1].

The pervaded volume available for the conformation of a polymer chain decreases when the chain becomes confined to dimensions smaller than its characteristic size scale d_{ee} in the bulk state[1, 2, 3, 4, 5]. Direct experimental observations suggest that the mobility of polymer chains near a free surface can exceed that in the bulk by several orders of magnitude [6], and this is ascribed to the reduced interchain entanglement density at the free surface [2, 4]. In the ultrathin film state, the reduction in interchain entanglement density and the increase in chain mobility are accompanied by a depression in the glass transition temperature T_g [7, 8] and a reduction in the tensile strength and ductility [9, 10, 11]. For example, the value of T_g of supported polystyrene (PS) films [7] and of supported cross−linked polyfluorene films [12] decreases as the film thickness decreases. The same behaviour is noted for free−standing PS films [8] and for free−standing polymethyl methacrylate (PMMA) films [13]. The uniaxial tensile strength and failure strain of water−supported PS films [9, 10] and of water−supported bisphenol-A polycarbonate films [11] drop sharply when the film thickness is reduced below the characteristic size d_{ee} of the polymer chain in the bulk state.

In the present study, we use molecular dynamics (MD) simulations to explore the thickness-dependent mechanical behaviour of linear and side-branched PMMA films over a wide range of temperatures (relative to T_g). Although the mechanical properties of linear PMMA in bulk form have been studied over a broad range of loading conditions by means of experiments [14, 15, 16], phenomenological constitutive modelling [17, 18, 19, 20], and by computer simulations [21, 22, 23, 24, 25, 26], the mechanical characterisation of molecularly confined PMMA structures, such as an ultrathin film, is currently limited. The mechanical response of this film is of direct relevance to industries ranging from electronics to the nanofoaming of polymers; at the end of the present study, a case study is presented on PMMA nanofoams and the close link between foamability and the tensile ductility of a thin film under equi-biaxial straining is quantified.

With the continuing improvements in computer hardware, software, and in simulation methodologies, MD simulations have evolved to become a very powerful tool for exploring the relationship between microstructure and properties [27, 28, 29, 30]. In essence, MD simulations solve Newton's second law of motion for a system of interacting particles [31, 32]. An important application is the prediction of the atomistic/molecular−level response of materials to complex thermo−mechanical loadings that are not easily measured experimentally. In the present study, MD simulations make use of the classical MD simulation code LAMMPS [33] from Sandia National Laboratories to probe the sensitivity of tensile response of ultrathin PMMA films to thickness, temperature, molecular weight, and to the degree of side-branching. In order to explore how molecular confinement and chain entanglement affect the mechanical response, we build molecular systems of various molecular arrangement and size. Specifically, we consider films composed of monodisperse bead−spring chains of molecular structure comprising $100-1000$ monomers per backbone, and $0-1500$ monomers per side-branch. The structural details of the linear and side-branched PMMA chains are sketched in Fig. 1. The film is subjected to in-plane uniaxial and equi-biaxial straining at a constant true strain rate of $10^8 \mathrm{s}^{-1}$.

1.1. Scope of study

First, the generation of molecular models is explained for linear and side-branched PMMA films. The main MD simulations are then presented for determining the glass transition temperature, and for in-plane tensile straining. The methods for evaluation of the macroscopic stress and strain states from the MD calculations are introduced. The large deformation response of the PMMA films to uniaxial and equi-biaxial tensile straining is reported for a film thickness h in the range 2.4 nm to 51 nm (giving $0.08 \leq h/d_{ee} \leq 1.10$), and a temperature T in the range 300 K to 600 K (giving $0.76 \leq T/T_g \leq 1.79$). The true stress versus true strain responses are determined, and an emphasis is placed on the sensitivity of ductility (defined by the strain at peak stress) to film thickness, temperature, molecular weight, and to the degree of side-branching. The practical usefulness of the results is then illustrated by a nanofoaming case study: we make use of the thickness−dependent tensile ductility to provide molecular−level insight into the rupture of cell walls during solid−state

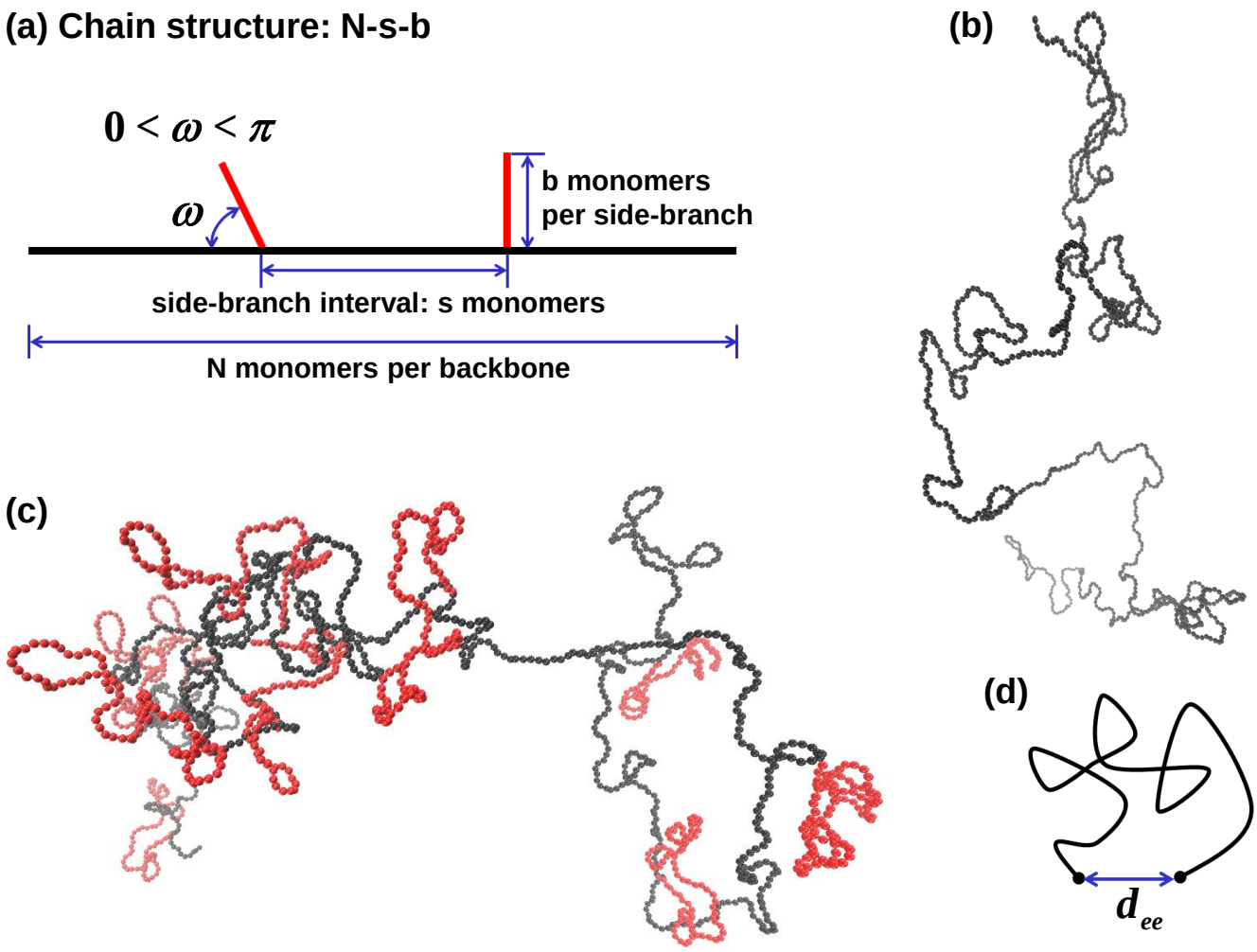

Figure 1: (a) A sketch of the side-branched PMMA chain structure. The coarse−grained bead−spring models of (b) a linear chain (N-s-b: 1000-0-0) and (c) a side-branched chain (N-s-b: 1000-100-100). The colours black and red denote the backbone chains and the side-branches, respectively. Molecular structures are visualised using VMD [34]. (d) A sketch of d_{ee} denoting the root−mean−square, end−to−end distance of a linear polymer chain in the bulk state.

nanofoaming of PMMA. The results support the hypothesis that cell wall tearing accounts for the observed limit in maximum attainable porosity [35].

2. Materials and methods

2.1. Molecular models and MD simulation setup

A coarse−grained, Kremer−Grest bead−spring model is adopted, in which a polymer chain is treated as a string of beads, with one bead representing one monomer, connected by elastic springs. A sketch of the side-branched chain structure, and the associated notation

$N-s-b$, are given in Fig. 1a, where the number of monomers per backbone is N, the side-branching interval is s monomers, and the number of monomers per side-branch is b. The bead−spring models of a linear chain (N-s-b: 1000-0-0) and a side-branched chain (N-s-b: 1000-100-100) are illustrated in Fig. 1b and Fig. 1c, respectively.

In MD simulations, particles in the simulation box (see Fig. 2a) are subjected to forces as defined via a set of interaction potentials (see Fig. 2b). The motion of the particles is tracked, and the interaction forces are updated based on the current positions of the particles. As a result, the output of an MD simulation is the history of particle positions. For all simulations in the present study, the equations of motion are integrated using the velocity Verlet algorithm with a time step of 7.6 fs [36]. The temperature and pressure are controlled by employing a Nose−Hoover thermostat and a Nose−Hoover barostat with a thermostatting damping parameter of 760 fs and a barostatting damping parameter of 7600 fs [33].

The non−bonded beads interact via a shifted Lennard−Jones (LJ) potential U_{NB} [36, 37] of the form

$$U_{NB}(r) = 4\varepsilon\left[\left(\frac{D}{r}\right)^{12} - \left(\frac{D}{r}\right)^{6}\right] + \varepsilon, \qquad r \le D_c \tag{1}$$
$$= 0, \qquad r > D_c$$

where r denotes the distance between two beads, $D = 0.5$ nm [38, 39] is the diameter of the bead, $\varepsilon = 1.65$ kcal/mole [38, 39] is the depth of the potential well, and $D_c = 1.25$ nm [38] is the cut-off distance for U_{NB}. The bonded beads along a chain are connected via a finite, extensible, nonlinear elastic (FENE) potential U_B [36, 37, 40] of the form

$$U_B(r) = -0.5\alpha R_o^2 \ln\left[1 - \left(\frac{r}{R_o}\right)^2\right] + \left\{4\varepsilon\left[\left(\frac{D}{r}\right)^{12} - \left(\frac{D}{r}\right)^{6}\right] + \varepsilon\right\}, \tag{2}$$

where $\alpha = 198.55$ kcal/(mole $\times$ nm^2) [36, 38] denotes the spring constant. On the right hand side of equation (2), the value of r in the first attractive term extends to $R_o = 0.75$ nm [36, 38], the maximum extent of the bond; the term inside the large curly brackets is a LJ repulsive term of cut-off distance $2^{1/6}D = 0.56$ nm [36, 37]. The choice of parameters

ensures that two chains cannot cross each other in dynamic simulations.

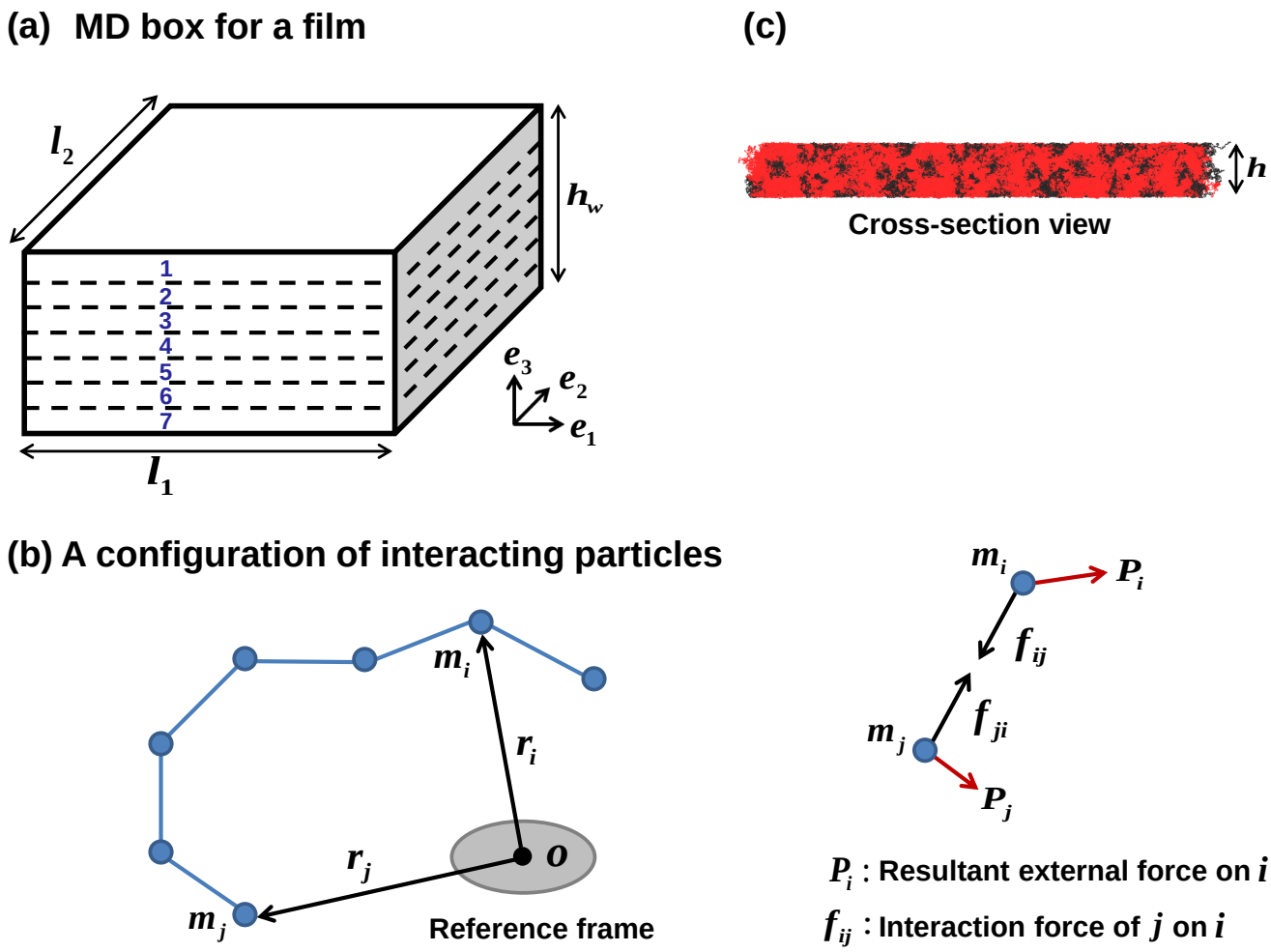

Figure 2: (a) A sketch of an MD simulation box containing a patch of PMMA film. The film is visually sliced into seven layers (1 to 7), of equal layer thickness, for tracking their layer−resolved microstructural evolution during the simulation. Layer 1 and Layer 7 correspond to the free surface layers of the film. (b) A configuration of an MD simulation system consisting of interacting particles. (c) Cross−section view of an equilibrated PMMA film, of thickness $h = 24$ nm, composed of monodisperse side-branched chains (N-s-b: 1000-500-1500). The colours black and red denote the backbone chains and the side-branches, respectively.

2.1.1. Preparation of the PMMA film

To imitate a film, the boundary conditions throughout this study are set to be periodic in directions 1 and 2 (in-plane) and non-periodic in direction 3 (along thickness) of the simulation box, see Fig. 2a. A box of monodisperse bead−spring chains of structure $N-s-b$ are constructed by using the Polymer Modeler tool [41]. This initial configuration, in which chain segments may be in close contact or overlapping, typically corresponds to a high energy

state, and consequently this initial configuration is first optimised by energy minimisation. The resulting structure is then subjected to two steps of equilibration by following the procedures in Ref. [42], in order to obtain an equilibrated free−standing polymer film.

For the first step of equilibration, two walls are introduced on the bottom and top faces of the simulation box, respectively, parallel to the $1-2$ plane, with a wall−to−wall distance h_w. The wall interacts with the particles by generating a force on the particle in a direction perpendicular to the wall. The particle−wall interaction energy is modelled by a 9−3 LJ potential [42], as given by

$$U_w(z) = \varepsilon_w \left[\left(\frac{D}{z} \right)^9 - \left(\frac{D}{z} \right)^3 \right], \tag{3}$$

where z denotes the distance from the particle to the wall in the 3−direction, $D = 0.5$ nm [38, 39] is the diameter of the bead, and $\varepsilon_w = 4.95$ kcal/mole [42] is the potential strength. The confined film is equilibrated under isothermal and isobaric conditions (an NPT computation) at a constant temperature $T = 600$ K (which is far above the value of T_g) and at a constant pressure $P_o = 0$ Pa. It is found that the box dimensions, value of h_w, and the conformational characteristics and stress state of individual chains (as defined in Refs. [28, 30]) all become stable at the desired temperature and pressure during the final 50 ns of this equilibration run. This ensures the equilibrium status of a confined film.

For the second step of equilibration, the equilibrated configuration of the confined film is used to prepare a film with two free surfaces. The particle−wall interaction potential at both walls is removed, and the resulting film system is equilibrated with the temperature and pressure maintained constant at $T = 600$ K and $P_o = 0$ Pa, respectively. The dimensions of the simulation box are adjusted independently in directions 1, 2, and 3 during barostatting. Again, the equilibration process is monitored by inspecting the box's dimensions and volume, and the chain's stress state and conformational characteristics (as defined in Refs. [28, 30]). These measures remain constant during the final 50 ns of this equilibration step, indicating that the equilibrium state of a free−standing film system has been reached at the desired temperature and pressure. The in-plane dimensions (l_1 and l_2) of the equilibrated simulation box are sufficiently large (greater than 170 nm) to minimise any artifacts associated with

periodic boundary conditions.

The film thickness h, as given by equation (S.5), is determined by following the definition in Ref. [42, 43] via the method of Gibbs dividing surface (GDS) [44], see SI for more details. It is instructive to non-dimensionalise the film thickness h by the root−mean−square end−to−end distance d_{ee}, a measure of the characteristic length scale of a polymer backbone chain in the bulk state, see Fig. 1d. In the present study, a freely rotating chain model is used, giving $d_{ee} = l\sqrt{C_\infty N}$, where N is the number of monomers along the backbone, l denotes the monomer length, and the characteristic ratio C_∞ equals 9.1 [45] for bulk PMMA. The MD-predicted distribution of d_{ee} for the individual chains in the film state is almost the same as that in the bulk state, indicating that the presence of a free surface has a negligible effect upon the magnitude of d_{ee}; this is consistent with the directly measured values of d_{ee} for the individual PMMA chains in an ultrathin film by scanning near-field optical microscopy [46] and by super-resolution fluorescence microscopy [47].

A cross-sectional view of an equilibrated free−standing PMMA film, of thickness $h = 24$ nm, is shown in Fig. 2c, for the case of monodisperse side-branched chains of type N-s-b: 1000-500-1500. These PMMA films (equilibrated at $T = 600$ K) are quenched in a series of isobaric runs, each at a cooling rate of 3.95 K/ns, in which the temperature is continuously decreased from $T = 600$ K to an intermediate temperature of $T = 520$ K, 410 K, 375 K, 345 K, and then to $T = 300$ K; the Nose−Hoover thermostat and barostat are used to adjust the temperature and maintain the pressure constant at $P_o = 0$ Pa. The configurations obtained upon cooling are further equilibrated by thermostatting at their respective temperatures and barostatting at $P_o = 0$ Pa. Equilibrium is attained after the box sizes, density, stress state, and the chain deformations become stable. These equilibrated configurations produced at each temperature then serve as the starting points for subsequent simulations of tensile straining.

2.2. Dependence of glass transition temperature T_g upon film thickness

The polymer film dilates with increasing temperature, due to thermal expansion. The transition between the glassy state and the liquid can thus be identified by the change in the temperature dependence of the volume. To determine the glass transition temperature

T_g of the film, the mass density ρ of the film is continuously monitored throughout cooling the polymer from $T = 600$ K in a viscous melt state to $T = 300$ K in a glassy state with a constant cooling rate 3.95 K/ns, and plotted as a function of temperature T. By following the procedure commonly employed in calorimetry experiments [48], two straight lines are fitted to the glassy and the viscous melt regimes, respectively, of the ρ versus T curve. The value of T_g is identified by the extrapolated intersection of these two linear lines, that is, when the slope of ρ changes [42, 49]. The slopes reflect the difference in thermal expansion coefficient between the melt and glassy regimes. For both experimental and simulation data, the choice of defining which portions of the curve are glassy and melt for the linear fitting can lead to significantly different estimates of T_g for the same sample [42, 49]. Here, we maintain a consistent T interval within which data are fitted for all films and bulk systems, resulting in an error of T_g within ± 17 K. This error does not affect the qualitative dependence of T_g upon film thickness h.

For a given chain structure N-s-b, the value of T_g decreases in an almost linear fashion with decreasing film thickness, see Fig. 3a. This thickness dependence of T_g is qualitatively similar to that observed for free−standing linear (N-s-b: 1590-0-0) PMMA films [13] by transmission ellipsometry at a cooling rate of 0.5 to 2.0 K/min; the comparison is shown in Fig. 3a. The qualitative dependence of T_g upon film thickness is also consistent with the MD-predicted trends reported in Ref. [38, 42] based upon a similar coarse−grained bead−spring model for PMMA. Due to the rapid cooling, the MD-predicted value of T_g exceeds the experimentally measured values for systems of comparable molecular weight. For bulk polymers, a 5 K to 10 K rise in T_g is expected per decade of increase in the cooling rate, which has been observed in other polymeric MD systems such as polycarbonate [30]. Since the cooling rate applied in the current study (3.95 K/ns) is about 9 orders of magnitude higher than that in experiments, this largely explains the difference between the predicted and the measured T_g values in Fig. 3a.

The through−thickness, layer−resolved, distribution of mass density ρ, from the individual layers of equal layer thickness (1 to 7, recall Fig. 2a), is shown in Fig. 3b for a linear (N-s-b: 1000-0-0) PMMA film of thickness $h = 25$ nm during cooling from $T = 600$ K ($T/T_g = 1.58$) to $T = 300$ K ($T/T_g = 0.79$). The layer thickness is $h/7 = 3.57$ nm. The

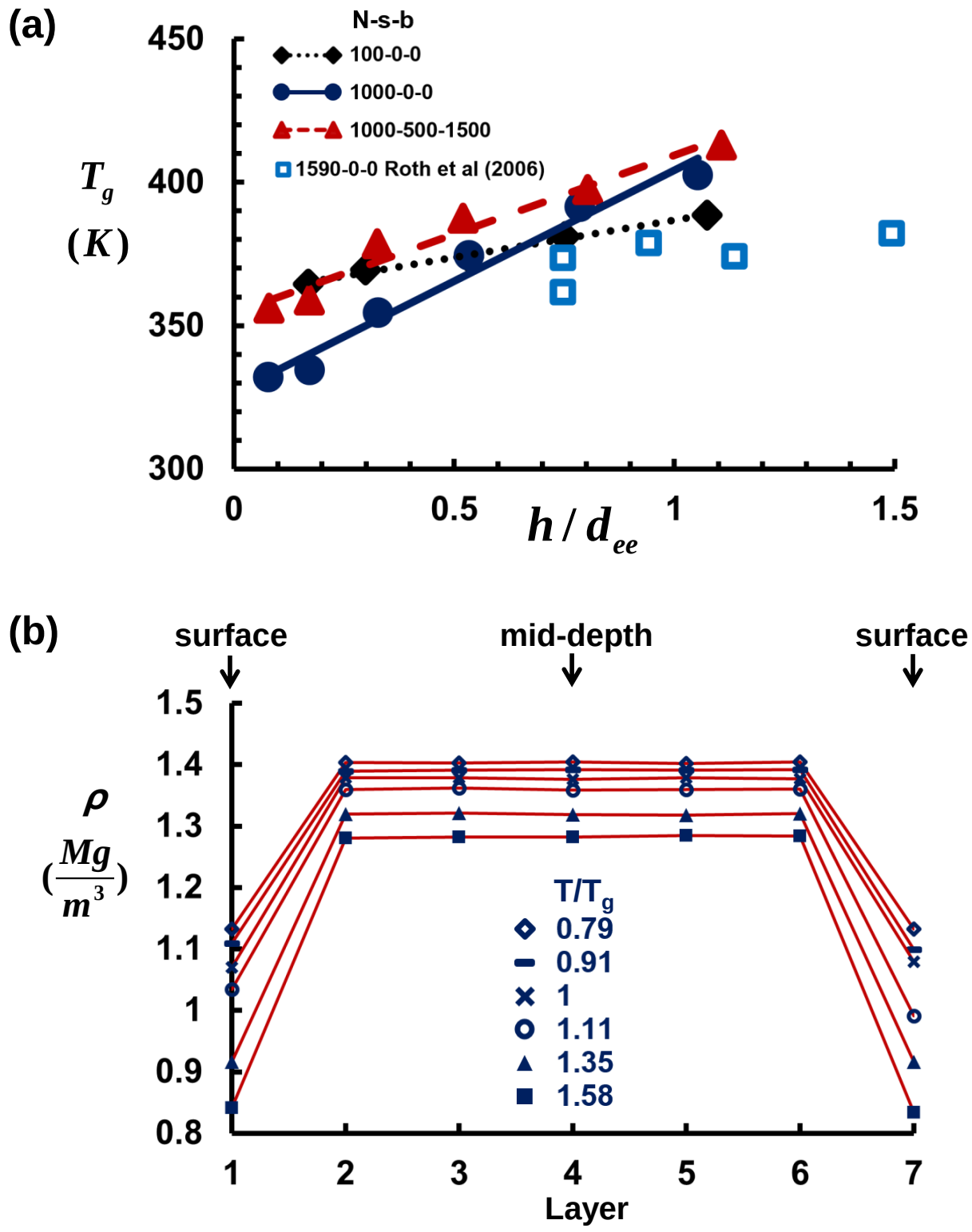

Figure 3: (a) The sensitivity of glass transition temperature T_g to film thickness h/d_{ee}. The measured T_g data for the free−standing (N-s-b: 1590-0-0) PMMA films are extracted from Roth et al. [13]. (b) Layer−resolved mass density ρ profile, of individual layers (1 to 7) with equal thickness, within a linear (N-s-b: 1000-0-0) PMMA film of thickness $h = 25$ nm, during cooling from $T = 600$ K to $T = 300$ K. The individual layer thickness is $h/7 = 3.57$ nm. The MD-predicted T_g value is 379 K for the overall film.

MD-predicted T_g value of the overall film is 379 K. For reference, the MD-predicted and the measured T_g values of PMMA in bulk form are 417 K (for N-s-b: 1000-0-0) and 388 K (for N-s-b: 924-0-0 by differential scanning calorimetry at a heating rate of 10 K/min [35]), respectively. At each value of T/T_g, the mass density of the free surface layers (1 and 7) is markedly less than that of the inner layers (2 to 6), implying that the molecular free volume and the molecular mobility of the free surface layers are greater than the interior to the film. This increase in molecular free volume and molecular mobility near a free surface is the primary reason for the depression in T_g [42, 43] and for the thickness dependence in the mechanical response of ultrathin polymeric films. At each value of T/T_g, the mass density of the mid-depth layer (layer 4) of the film is very close to the corresponding bulk density under the same simulation conditions, consistent with the MD-predicted density profiles reported in Ref. [42] based upon a similar coarse−grained, bead−spring, polymer model.

2.3. MD simulations of in-plane tensile straining

Based upon the equilibrated configuration of the free−standing PMMA film system, the simulation box is stretched in direction 1 in uniaxial tension, or in directions 1 and 2 in equi-biaxial tension, at a constant true strain rate of $10^8 \mathrm{s}^{-1}$, with the temperature maintained constant by employing a Nose−Hoover thermostat. In-plane, periodic boundary conditions are enforced. The faces of the film are treated as free surfaces with non-periodic boundary conditions applied along the thickness direction.

We focus on the response of virial stress $\boldsymbol{\sigma}_t$ as given by

$$\boldsymbol{\sigma}_t = \frac{1}{V_t} \sum_{i \in \Omega} \left[\frac{1}{2} \sum_{j \in \Omega, j \neq i} (\mathbf{r}_j - \mathbf{r}_i) \otimes \mathbf{f}_{ij} - m_i \tilde{\mathbf{v}}_i \otimes \tilde{\mathbf{v}}_i \right], \tag{4}$$

where V_t is the volume of the total system, $\tilde{\mathbf{v}}_i$ is the thermal excitation velocity of particle i, and "$\otimes$" denotes the tensor product, see SI for more details. We take this stress as a measure of the continuum-level Cauchy stress, see Refs [28, 50, 51] for the definitions and interpretation of other local mechanical stresses. In the present study, we shall make use of the non-dimensionalised virial stress $\boldsymbol{\sigma}_t/\sigma_o$, where $\sigma_o = \varepsilon/D^3$ (and $D = 0.5$ nm, $\varepsilon = 1.65$ kcal/mol) for the modelled PMMA systems. The macroscopic measure of strain is based on

the deformation of the simulation box. The true (logarithmic) tensile strain in the loading direction 1 is $\epsilon_{t1} = \ln(l_1/L_1)$, where, L_1 and l_1 denote the length of the simulation box in the reference and current configurations, respectively. For equi-biaxial tension, one has $\epsilon_{t2} = \epsilon_{t1}$. The von Mises effective strain ϵ_e is defined in the usual manner as $\epsilon_e^2 = (2/3)\epsilon_{ij}\epsilon_{ij}$. Note that the effective strain simplifies to $\epsilon_e = \epsilon_t$ for uniaxial tensile straining $\epsilon_{t1} = \epsilon_t$, and to $\epsilon_e = 2\epsilon_t$ for equi-biaxial tensile straining $\epsilon_{t1} = \epsilon_{t2} = \epsilon_t$ upon assuming incompressibility.

The deformation gradient $\mathbf{F}$ is calculated by using the "MinD" method (see Refs. [28, 52] for pertinent details), which is based on the idea of minimising the difference between the MD measure for deformation and its continuum counterpart for an arbitrary subset of an MD system. The dilatation of a stack of layers within a film is given in terms of the volume ratio $V/V_o = \det(\mathbf{F})$, where V and V_o denote the volume in the current and the initial configurations, respectively.

3. Results and discussion

The MD-predicted true stress versus true strain responses are now presented for the PMMA films subjected to uniaxial and equi-biaxial tensile straining. The sensitivity of the tensile strength and ductility to temperature, thickness, molecular weight, and to the degree of side-branching is reported. Representative snapshots of the microstructures reveal the conformational evolution of individual chains with increasing macroscopic strain. Chain scission (breakage of covalent bonds) is not modelled in the current study, and macroscopic failure is by the breakdown of entangled polymer networks via disentanglement. As a specific application of the study, we shall make use of the MD-predicted, thickness-dependent tensile ductility to predict the maximum achievable porosity of PMMA nanofoams as produced by solid-state nanofoaming.

3.1. Dependence of the uniaxial and equi-biaxial tensile responses upon temperature

The sensitivity of the uniaxial and equi-biaxial tensile responses to temperature (relative to T_g) is investigated for the linear and side-branched PMMA films; the temperature is in the range $T = 300$ K to $T = 600$ K, such that T/T_g ranges from 0.76 to 1.79.

For illustration, the non-dimensional nominal stress σ_n/σ_o and the non-dimensional true stress σ_t/σ_o are plotted as a function of the true tensile strain ϵ_t in Fig. 4a for a linear (N-s-b: 1000-0-0) PMMA film of thickness $h = 24.5$ nm, at $T/T_g = 0.80$. The end-to-end separation of this polymer chain in the bulk state is $d_{ee} = 45.8$ nm, giving $h/d_{ee} = 0.53$. At $T = 300$ K ($T/T_g = 0.80$), the film is in the glassy regime; the true stress σ_t/σ_o exhibits a characteristic elastic-plastic response, with an initial elastic response followed by a distinct yield, immediate softening and subsequent strain hardening up to failure. The peak value of true stress, σ_{pk}/σ_o, is identified in Fig. 4a, and the corresponding true strain defines the true failure strain ϵ_f. Recall that the von Mises effective strain ϵ_e equals the uniaxial strain for an incompressible solid. Also note that the uniaxial nominal stress, σ_n/σ_o, has a peak value at a true tensile strain that is almost identical in value to ϵ_f. The equi-biaxial tensile failure strain is $\epsilon_f = 0.81$, and this implies that the von Mises effective strain ϵ_e at failure equals 1.62 upon assuming incompressibility. The higher value of ϵ_e in uniaxial tension than in equi-biaxial tension is associated with much greater orientation-hardening. We shall focus on the true tensile stress versus true tensile strain response in the remainder of this study for both uniaxial and equi-biaxial loading.

The layer−resolved dilatation, of a stack of layers (1 to 7, recall Fig. 2a) with equal layer thickness, within a film of thickness $h = 24.5$ nm, is expressed in terms of the volume ratio V/V_o, see Fig. 4b. The layer thickness is $h/7 = 3.5$ nm. The volumetric response of the outermost layers $(1, 7)$ differs markedly from that of the interior layers (2 to 6) due to the increased molecular free volume and molecular mobility at the free surfaces (recall Fig. 3b). As the macroscopic strain increases, the volume of the free surface layers reduces substantially, in contrast to the slight volume increase in the inner layers as shown in Fig. 4b. For example, for uniaxial tensile straining at $\epsilon_t = 1.5$ (less than the failure strain of 2.31), the average value of V/V_o equals 0.89 for the free surface layers $(1, 7)$, and equals 1.01 for the interior layers (2 to 6). In similar fashion, for equi-biaxial tensile straining at $\epsilon_t = 0.6$ (less than the failure strain of 0.81), the average value of V/V_o equals 0.87 for the free surface layers $(1, 7)$, and equals 1.03 for the interior layers (2 to 6). Beyond peak stress, all layers increase their volume as a result of molecular disentanglement.

The failure mechanism associated with voiding, as detailed below, is revealed by layer-

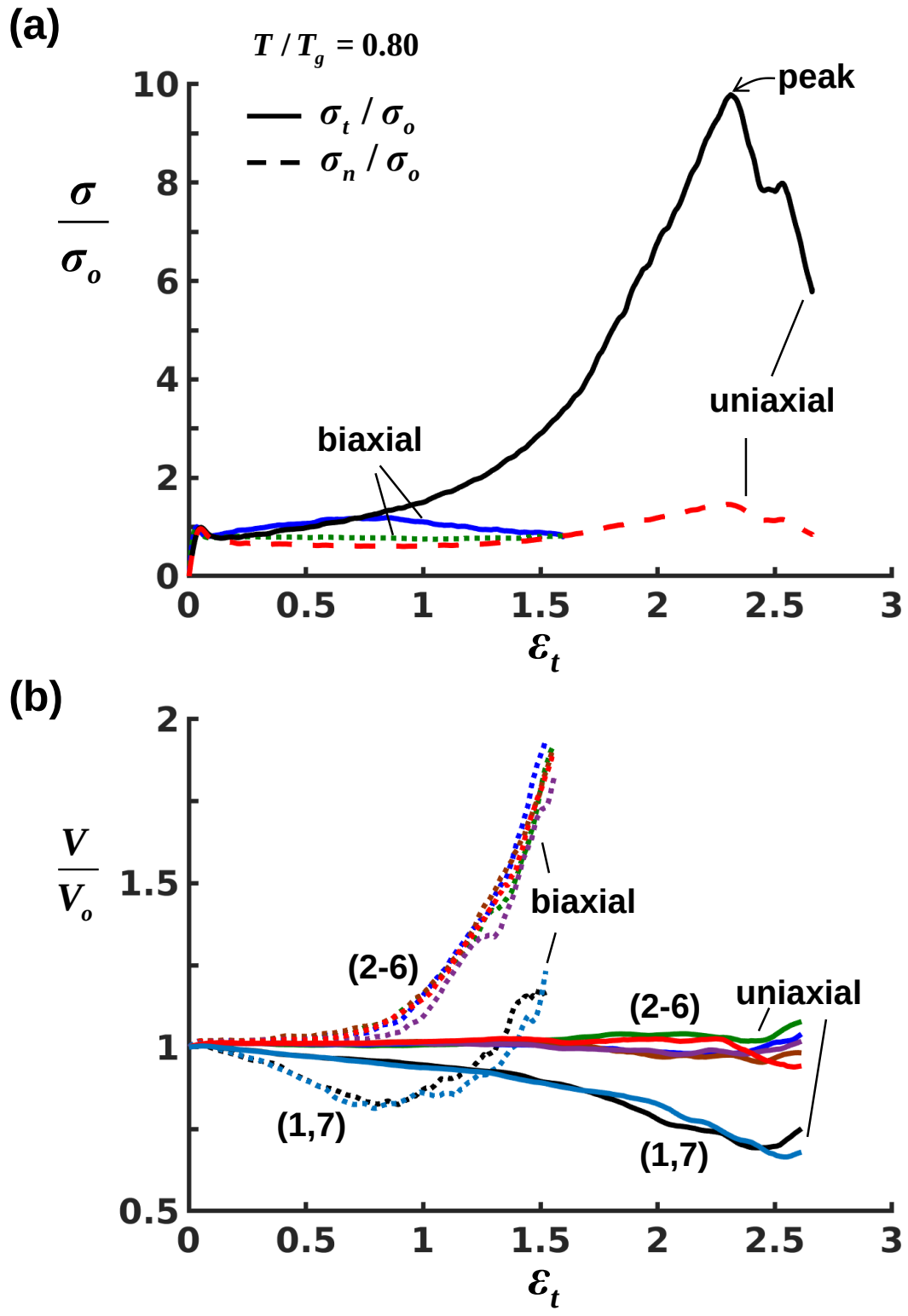

Figure 4: (a) The true stress versus true strain response of a linear (N-s-b: 1000-0-0) PMMA film, of film thickness $h = 24.5$ nm, subjected to uniaxial tensile straining $\epsilon_{t1} = \epsilon_t$ and equi-biaxial tensile straining $\epsilon_{t1} = \epsilon_{t2} = \epsilon_t$ at $T = 300$ K in the glassy regime for a constant true strain rate of $10^8 s^{-1}$. The corresponding non-dimensionalised nominal stress σ_n/σ_o is included for reference. (b) The layer−resolved volume ratio V/V_o, of the individual layers (1 to 7) with equal thickness $h/7 = 3.5$ nm, is plotted as a function of tensile strain.

resolved evolution of the microstructure through the thickness of the film during straining. The local density is evaluated for each layer throughout the straining process, and the location of voiding, where the local density drops substantially toward zero, is identified for each layer. As the macroscopic strain increases, small voids initiate randomly at the free surface layers $(1, 7)$, with no discernible voids present at mid-depth (layer 4), see Fig. 5a for uniaxial tension and Fig. 5b for equi-biaxial tension. The voids propagate in the through-thickness direction by growing in size and number, with subsequent void coalescence and ultimate failure. At large strains, a network of polymer molecules align along the straining direction, with disentanglemt of chains present in the vicinity of the voids.

The true stress versus true strain responses are explored at elevated temperatures for a linear (N-s-b: 1000-0-0) PMMA film of thickness $h = 24.5$ nm subjected to uniaxial tension (see Fig. 6a) and to equi-biaxial tension (see Fig. 6c) up to failure. Additional insight is obtained by interrupting the tensile straining prior to failure, and then unloading to zero strain. The true stress versus true strain curves for such a loading-unloading probing cycle are shown in Fig. 6b for uniaxial tension and in Fig. 6d for equi-biaxial tension.

The glassy regime exists for $T/T_g < 1$, and in this regime the PMMA film exhibits an initial, linear elastic response prior to yielding. The yield point is immediately followed by softening and by subsequent strain hardening, such that large plastic strains precede failure. For linear (N-s-b: 1000-0-0) PMMA films of thickness $h = 7.9$ nm, 24.5 nm, and 48.3 nm, the MD-predicted values of yield strain are almost constant at $\epsilon_t = 0.05$ in uniaxial tension, and $\epsilon_t = 0.03$ in equi-biaxial tension, for temperatures in the range $T = 300$ K to $T = 375$ K, (corresponding to $0.75 \leq T/T_g < 1$). In comparison, the linear (N-s-b: 924-0-0) PMMA in bulk form yields at $\epsilon_t = 0.07$ for $T = 363$ K ($T/T_g = 0.94$) and $T = 378$ K ($T/T_g = 0.98$) for the case of uniaxial tension at a nominal strain rate of $5.9 \times 10^{-2}\text{s}^{-1}$ [35]. Both the MD-predicted and the measured [35] values of yield stress decrease with increasing temperature. Within this glassy regime, unloading occurs in an elastic manner, which is characteristic of an elasto-viscoplastic solid, as shown in Figs. 6b and d, with a finite remnant strain at zero load. A substantial remnant compressive stress is observed upon unloading to zero strain.

Now consider the response near the glass transition temperature $T/T_g = 1$. The distinct yield point disappears in this glass transition regime. Unloading is accompanied by a sub-

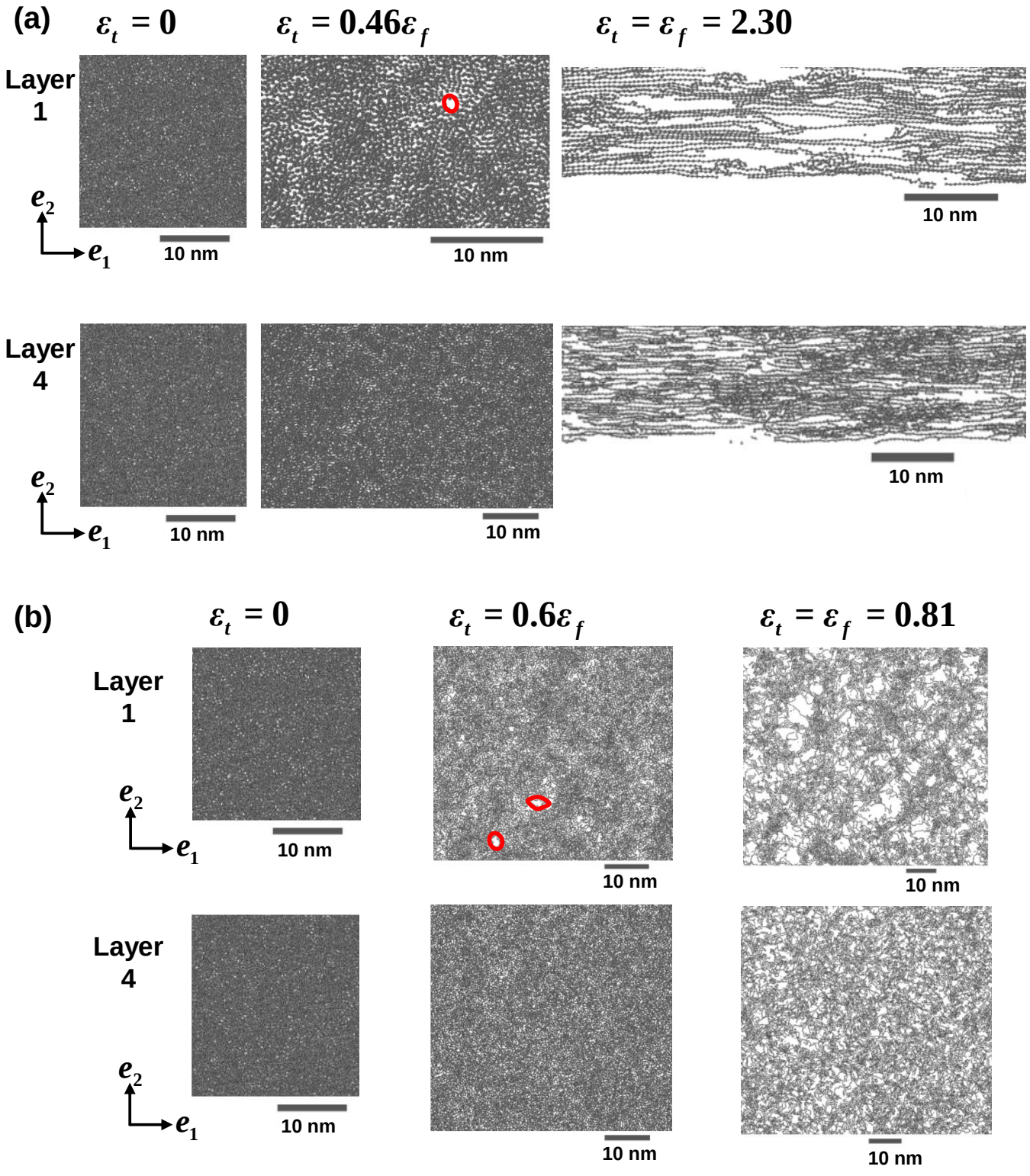

Figure 5: The microstructural evolution of the free surface layer (layer 1) and the mid-depth layer (layer 4) within a linear (N-s-b: 1000-0-0) PMMA film, of film thickness $h = 24.5$ nm, subjected to (a) uniaxial tensile straining $\epsilon_{t1} = \epsilon_t$ and (b) equi-biaxial tensile straining $\epsilon_{t1} = \epsilon_{t2} = \epsilon_t$ at $T = 300$ K (giving $T/T_g = 0.80$). The layer thickness is $h/7 = 3.5$ nm. Representative voids that randomly initiate first on the free surface layers are highlighted in red.

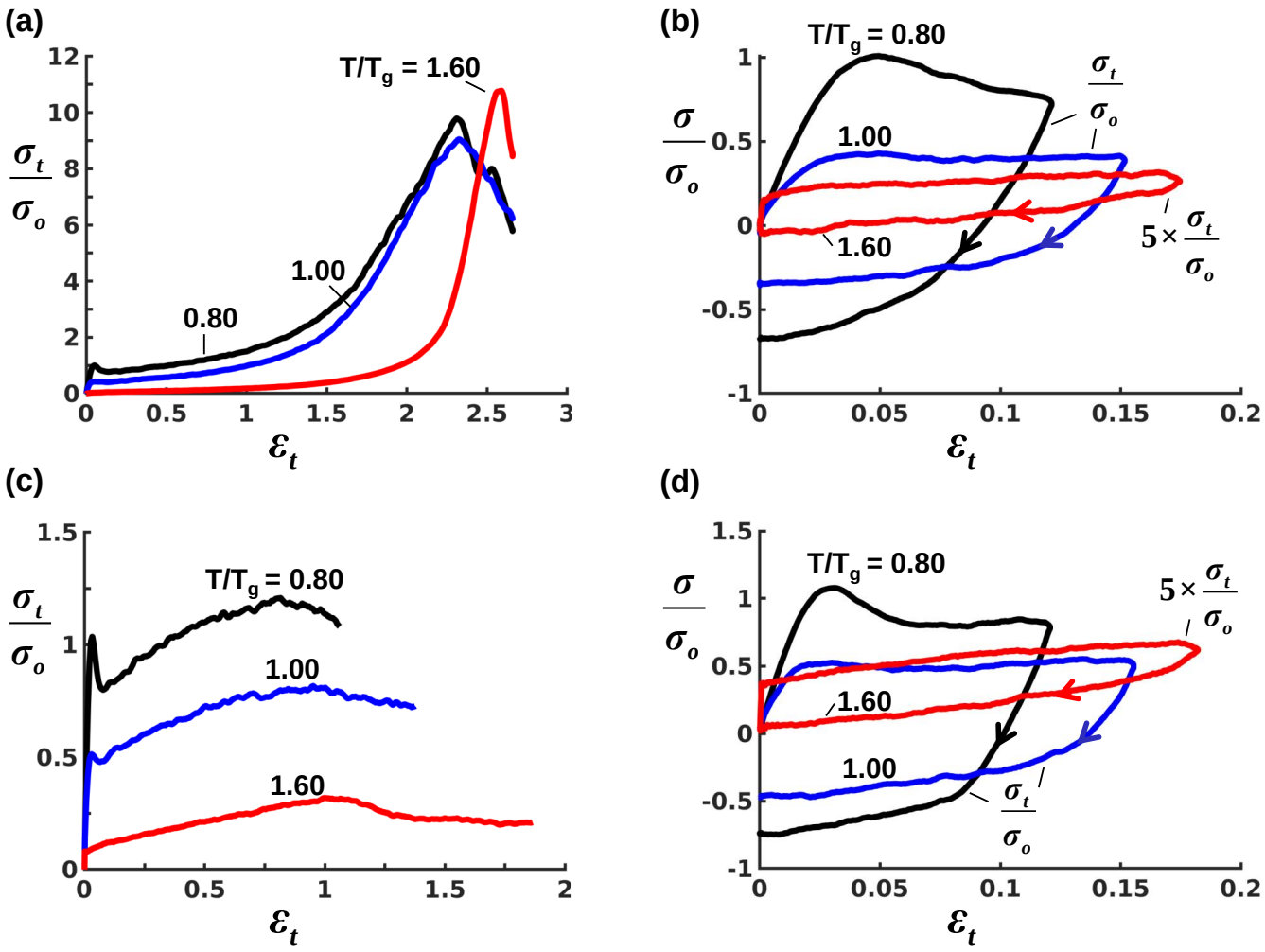

Figure 6: True stress versus true strain curves for (a) uniaxial tensile straining and (b) the associated loading-unloading cycle prior to failure; (c) equi-biaxial tensile straining and (d) the associated loading-unloading cycle prior to failure. Results are shown for a linear (N-s-b: 1000-0-0) PMMA film of thickness $h = 24.5$ nm at various temperatures.

stantial remnant strain at zero load and a finite remnant compressive stress at zero strain. At $T/T_g > 1$, the viscous regime is entered. Upon unloading at $T/T_g = 1.60$, the remnant strain at zero load reduces to almost zero, and consequently the remnant stress at zero strain is almost zero, see Figs. 6b and d.

The elastic rubbery regime, within which the unloading curve aligns with the elastic loading curve, may or may not exist depending upon the molecular weight of the polymer [53]. If it does exist then it does so above the glass transition and before entering the viscous regime. The rubbery regime is absent for PMMA grades of relatively low molecular weight, i.e., $M_w < 150$ kg/mol [53], but is present for PMMA grades of moderate to high molecular weight, for example, $M_w = 3,580$ kg/mol [16]. Note that the elastic rubbery regime above the glass transition is absent for the current linear (N-s-b: 1000-0-0) PMMA films. This is consistent with the experimentally observed response of the linear (N-s-b: 924-0-0) PMMA in bulk form [35].

The sensitivity of the tensile peak stress σ_{pk}/σ_o and the corresponding failure strain ϵ_f to T/T_g is assembled in Fig. 7a and Fig. 7b, respectively, for the linear (N-s-b: 1000-0-0) PMMA films of thicknesses $h = 7.9$ nm, 24.5 nm, and 48.3 nm. For a given value of T/T_g, both σ_{pk}/σ_o and ϵ_f decrease with decreasing thickness for both uniaxial and equi-biaxial tensile straining. For a given value of h, the value of σ_{pk}/σ_o is almost independent of T/T_g for uniaxial tension and decreases almost linearly with increasing T/T_g for equi-biaxial tension. In contrast, ϵ_f increases almost linearly with increasing T/T_g for both uniaxial and equi-biaxial tension: with increasing T/T_g, the enhanced segmental mobility facilitates the polymer molecules to rearrange and undertake large strains before ultimate failure intervenes. At a given temperature, the higher ductility in uniaxial tension than in equi-biaxial tension is associated with a higher uniaxial tensile strength.

In the glassy and glass transition regimes, the MD-predicted failure strain ϵ_f for the film exceeds that measured experimentally for the bulk; this is attributed to the fact that pre-existing defects are present in macro-scale specimens [16] but are absent in the current MD systems. For example, for the linear (N-s-b: 924-0-0) PMMA in bulk form, the measured true tensile failure strain ϵ_f decreases almost linearly from $\epsilon_f = 2.82$ at $T/T_g = 1.04$ to $\epsilon_f = 0.6$ at $T/T_g = 0.97$ in uniaxial tension at a nominal strain rate of $5.9 \times 10^{-2}\text{s}^{-1}$ [35]. In contrast, for

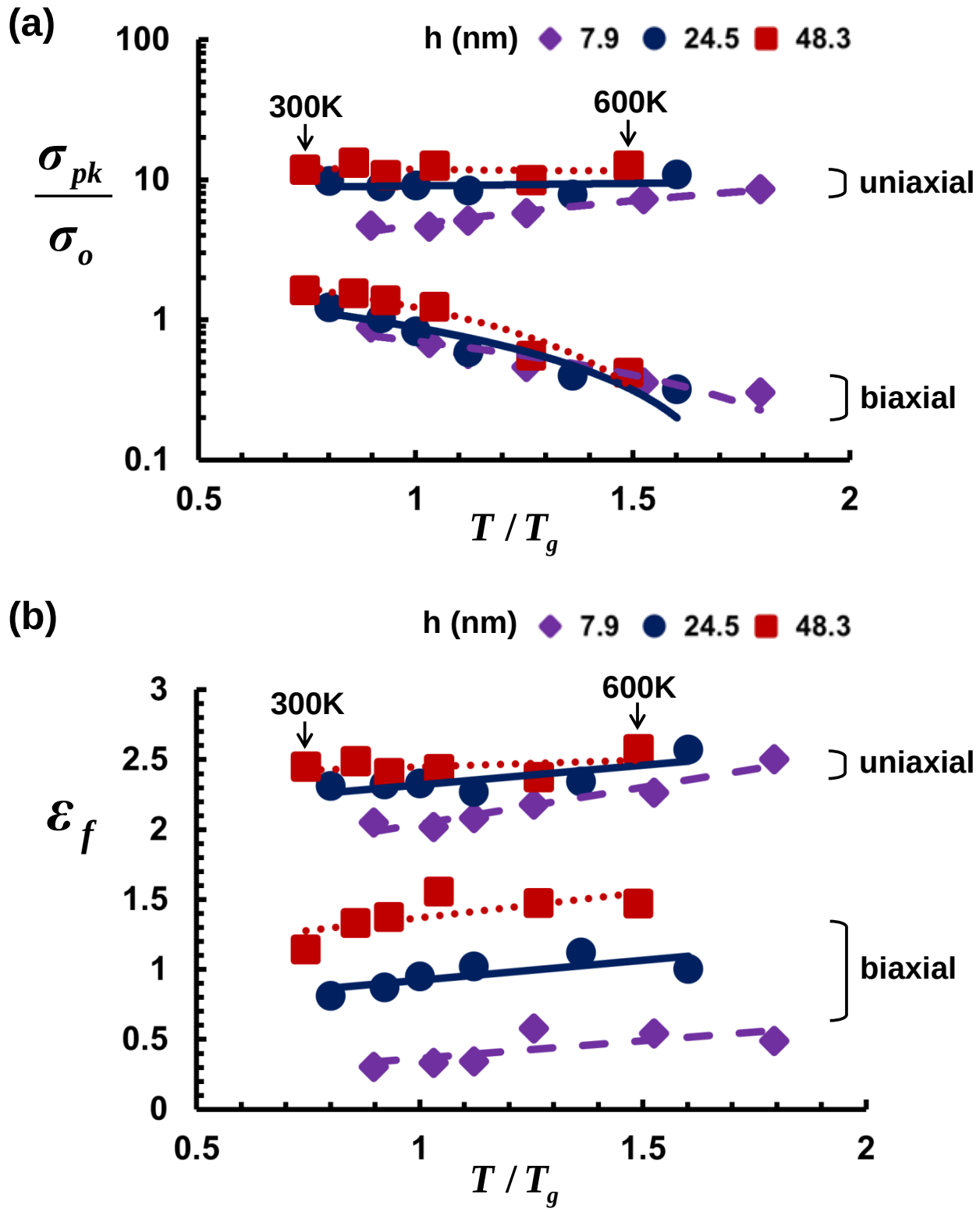

Figure 7: The effect of temperature T/T_g upon (a) the tensile peak stress σ_{pk}/σ_o and (b) the corresponding tensile failure strain ϵ_f. Results are plotted for linear (N-s-b: 1000-0-0) PMMA films, of thickness $h = 7.9$ nm, 24.5 nm, 48.3 nm, subjected to uniaxial and equi-biaxial tensile straining. Equations of the best fitting straight lines are described in Table 1 of SI.

a linear (N-s-b: 1000-0-0) PMMA film, of thickness $h = 48.3$ nm ($h/d_{ee} = 1.05$), subjected to uniaxial tension, the MD-predicted true failure strain ϵ_f decreases almost linearly from $\epsilon_f = 2.58$ at $T/T_g = 1.49$ to $\epsilon_f = 2.45$ at $T/T_g = 0.75$.

3.2. Sensitivity of tensile failure strain to film thickness

The sensitivity of the uniaxial and equi-biaxial tensile responses to film thickness is now explored for the linear and side-branched PMMA films at $T = 300$ K in the glassy regime and at $T = 600$ K in the viscous regime. The film thickness h ranges from 2.4 nm to 51 nm, and consequently h/d_{ee} ranges from 0.08 to 1.10.

The true tensile stress versus true tensile strain curves are shown in Fig. 8 for the linear (N-s-b: 1000-0-0) films over a wide range of thickness. The glassy regime exists at $T = 300$ K, and all films exhibit a typical elastic-plastic response both in uniaxial tension (see Fig. 8a) and in equi-biaxial tension (see Fig. 8b). In broad terms, the uniaxial response is almost independent of thickness h at both $T = 300$ K (Fig. 8a) and at $T = 600$ K (Fig. 8c). For equi-biaxial loading at $T = 300$ K, the yield strength is almost insensitive to increasing h whereas the degree of strain hardening prior to peak stress increases with increasing h (Fig. 8b). In contrast, for equi-biaxial loading at $T = 600$ K (Fig. 8d), the strain hardening rate is almost invariant but the yield strength decreases with increasing h.

In anticipation of the case study later in this study on the porosity limitation placed on nanofoaming by the drop in ductility with diminishing film thickness, we proceed to explore ϵ_f as a function of h/d_{ee} for three selected microstructures, as characterised by N-s-b. The dependence of tensile failure strain ϵ_f upon h/d_{ee} is summarised in Fig. 9a for $T = 300$ K and in Fig. 9b for $T = 600$ K for three choices of microstructure N-s-b. For a given chain structure N-s-b, ϵ_f decreases with decreasing h/d_{ee}. Now consider a fixed value of h/d_{ee}; then, ϵ_f decreases with decreasing backbone length of N monomers, but is almost insensitive to the degree of side-branching.

3.3. Sensitivity of tensile strength and ductility to temperature and to the degree of side-branching

For $N = 1000$ monomers per backbone, the sensitivity of the tensile response to the degree of side-branching is probed by varying the side-branching interval of s monomers and

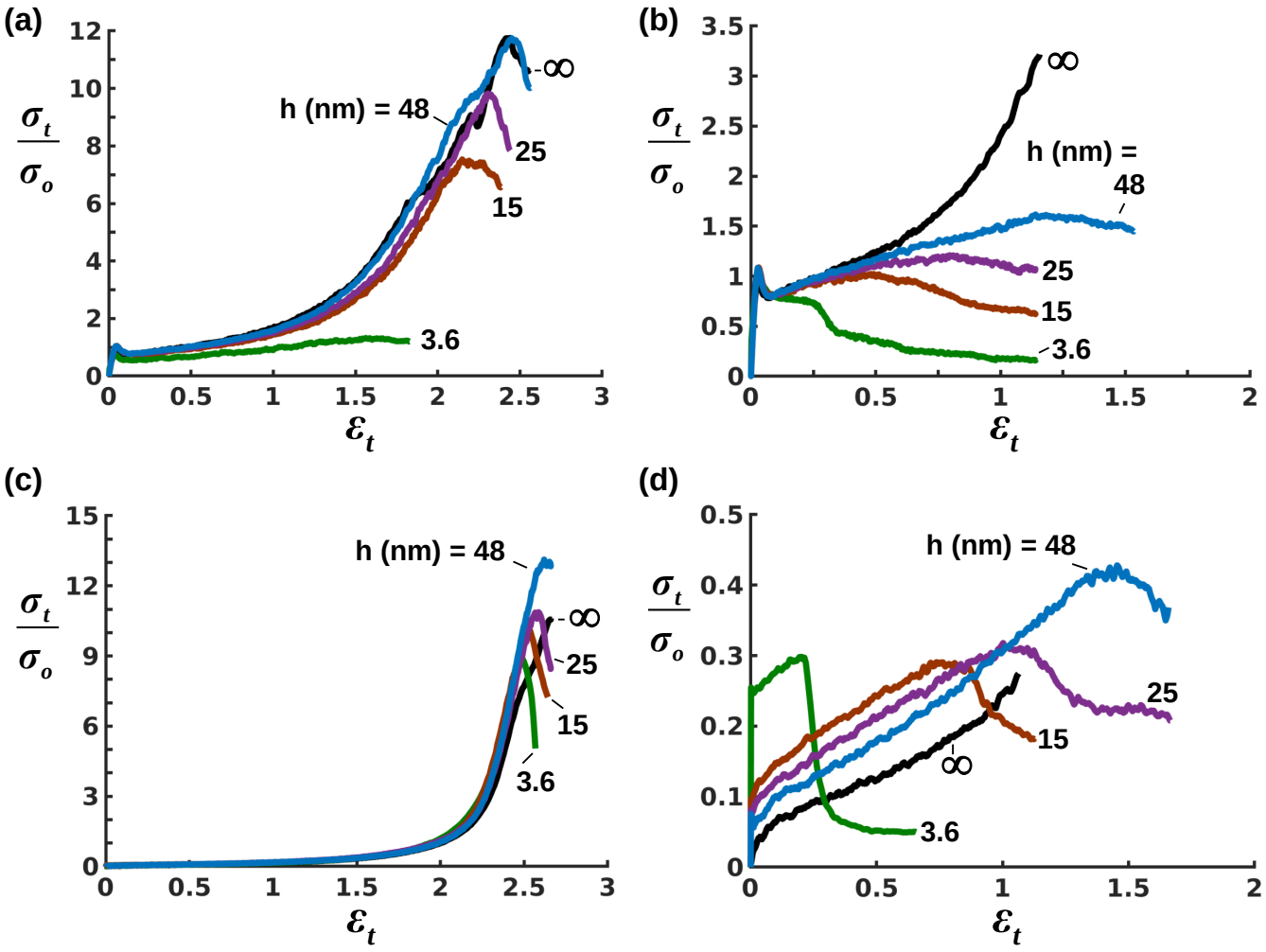

Figure 8: The true stress versus true strain curves of the linear (N-s-b: 1000-0-0) PMMA films of selected thicknesses subjected to (a) uniaxial tensile straining $\epsilon_{t1} = \epsilon_t$ and (b) equi-biaxial tensile straining $\epsilon_{t1} = \epsilon_{t2} = \epsilon_t$, both at $T = 300$ K in the glassy regime; (c) uniaxial tensile straining $\epsilon_{t1} = \epsilon_t$ and (d) equi-biaxial tensile straining $\epsilon_{t1} = \epsilon_{t2} = \epsilon_t$, both at $T = 600$ K in the viscous regime.

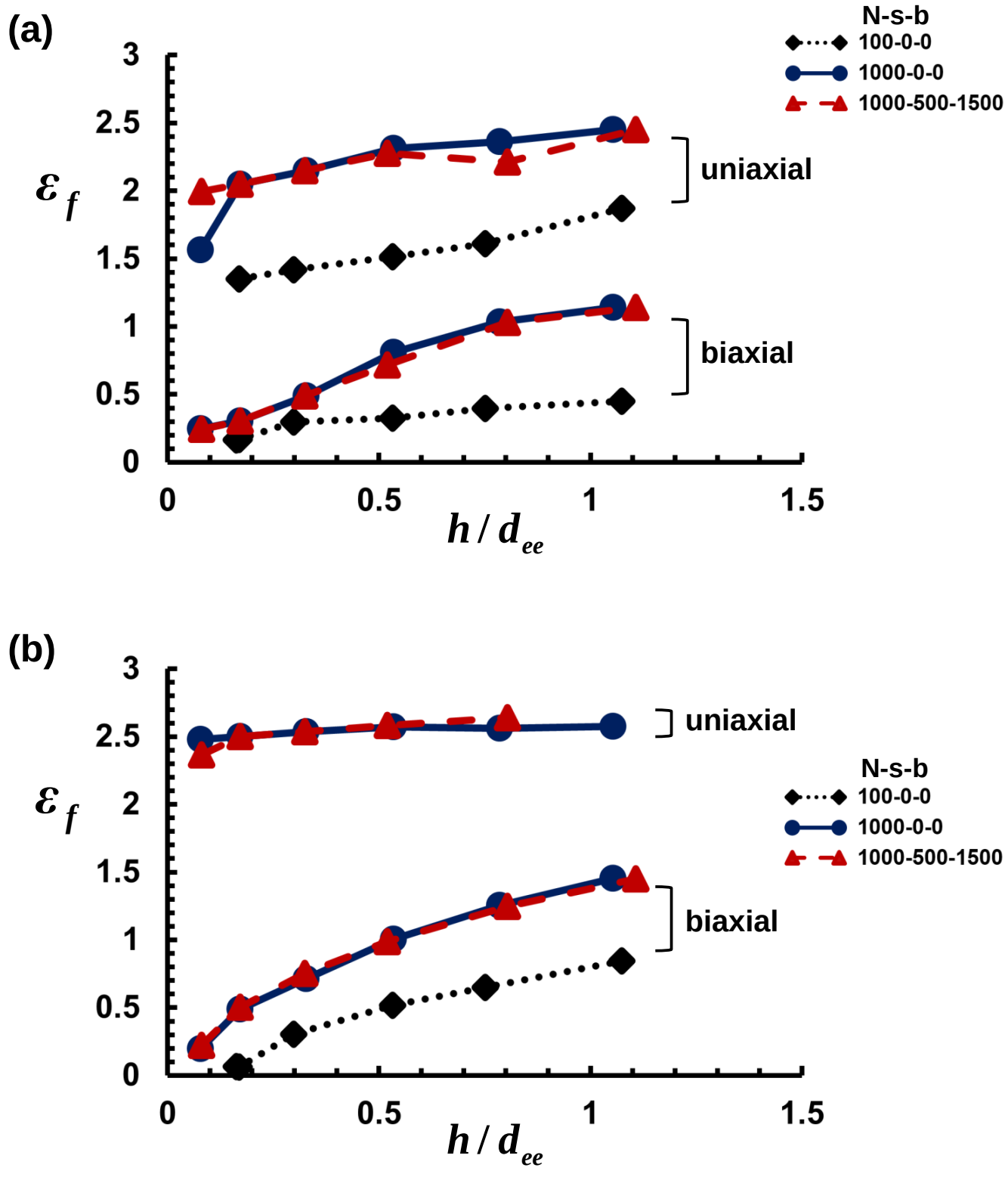

Figure 9: Tensile failure strain ϵ_f versus film thickness h/d_{ee} at (a) $T = 300$ K in the glassy regime and (b) $T = 600$ K in the viscous regime.

the side-branching length of b monomers. For $h = 24$ nm, the true stress versus true strain curves are shown in Fig. 10 for a uniaxial loading-unloading probing cycle in the glassy regime at $T = 300$ K ($T/T_g = 0.80$), at the glass transition $T = 375$ K ($T/T_g = 1$), and in the viscous regime at $T = 420$ K ($T/T_g = 1.12$) and at $T = 510$ K ($T/T_g = 1.36$). In all cases, the degree of side-branching plays a secondary role: the tensile stress-strain responses of the side-branched films do not deviate significantly from their linear counterparts. Within each regime, unloading is accompanied by a finite remnant strain at zero load, and by a finite remnant compressive stress at zero strain. The elastic rubbery regime above the glass transition is absent for these side-branched PMMA films. Consequently, the tensile strength and ductility, as shown in Figs. 11a and b, respectively, exhibit no substantial sensitivity to the degree of side-branching over the temperature range $0.76 \leq T/T_g \leq 1.60$.

4. Case study: sensitivity of achievable porosity of PMMA nanofoams to cell wall rupture

Polymeric nanofoams, of average cell size below 1 μm [54], have the potential to offer unique combinations of thermal, mechanical and optical properties [55]. Extrapolation of existing data suggests that the thermal conductivity of polymeric nanofoams may be lower than the value for air, 0.025 $\mathrm{Wm^{-1}K^{-1}}$, when the average cell size is below 200 nm and the porosity f exceeds 0.85 [56]. However, this ideal combination of high porosity and small cell size has not yet been achieved in practice [35, 54].

Solid-state nanofoaming experiments have been conducted by Van Loock et al. [35] on a linear PMMA grade, of chain structure (N-s-b: 924-0-0), using CO_2 as the blowing agent and a wide range of foaming conditions. The measured average cell size of the PMMA nanofoams is close to 250 nm and the attainable porosity is $f_{max} = 0.75$ [35]. The microstructure of the nanofoams transitions from closed-celled to open-celled at a porosity close to f_{max}. This observed limit in maximum achievable porosity has been interpreted in terms of cell wall failure; the existence of a minimum cell wall thickness, of magnitude close to that of the end-to-end distance d_{ee} of the individual polymer chains, has been suggested [35, 54]. Cell walls rupture as the cell wall thickness approaches this minimum value during nanofoaming; this leads to an open-celled microstructure, and consequently to a practical limit on foam

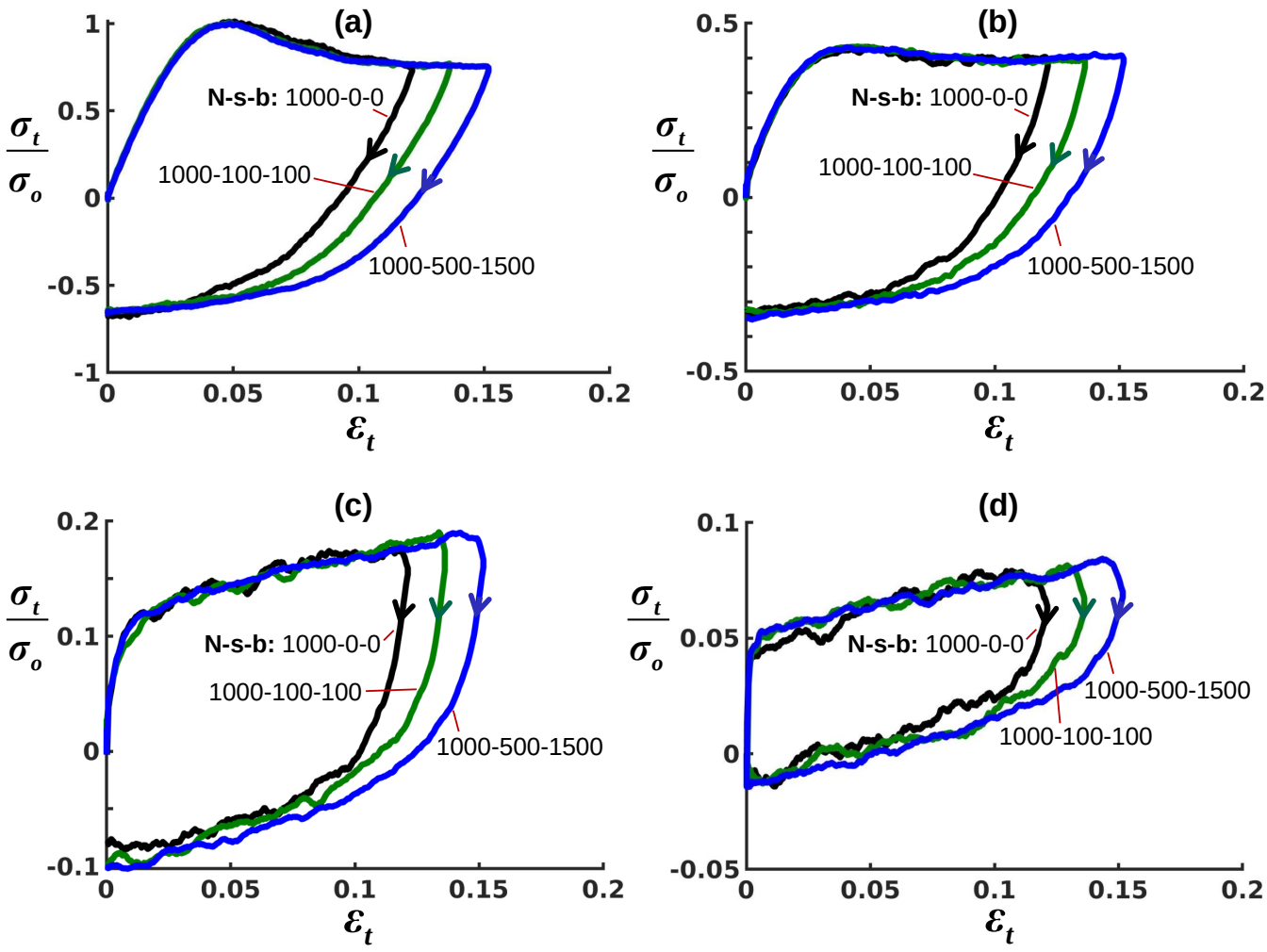

Figure 10: The effect of the degree of side-branching upon the true stress versus true strain curves at (a) $T = 300$ K, (b) $T = 375$ K, (c) $T = 420$ K, and (d) $T = 510$ K. Results are plotted for PMMA films, of thickness $h = 24$ nm, subjected to a uniaxial tensile loading-unloading cycle prior to failure.

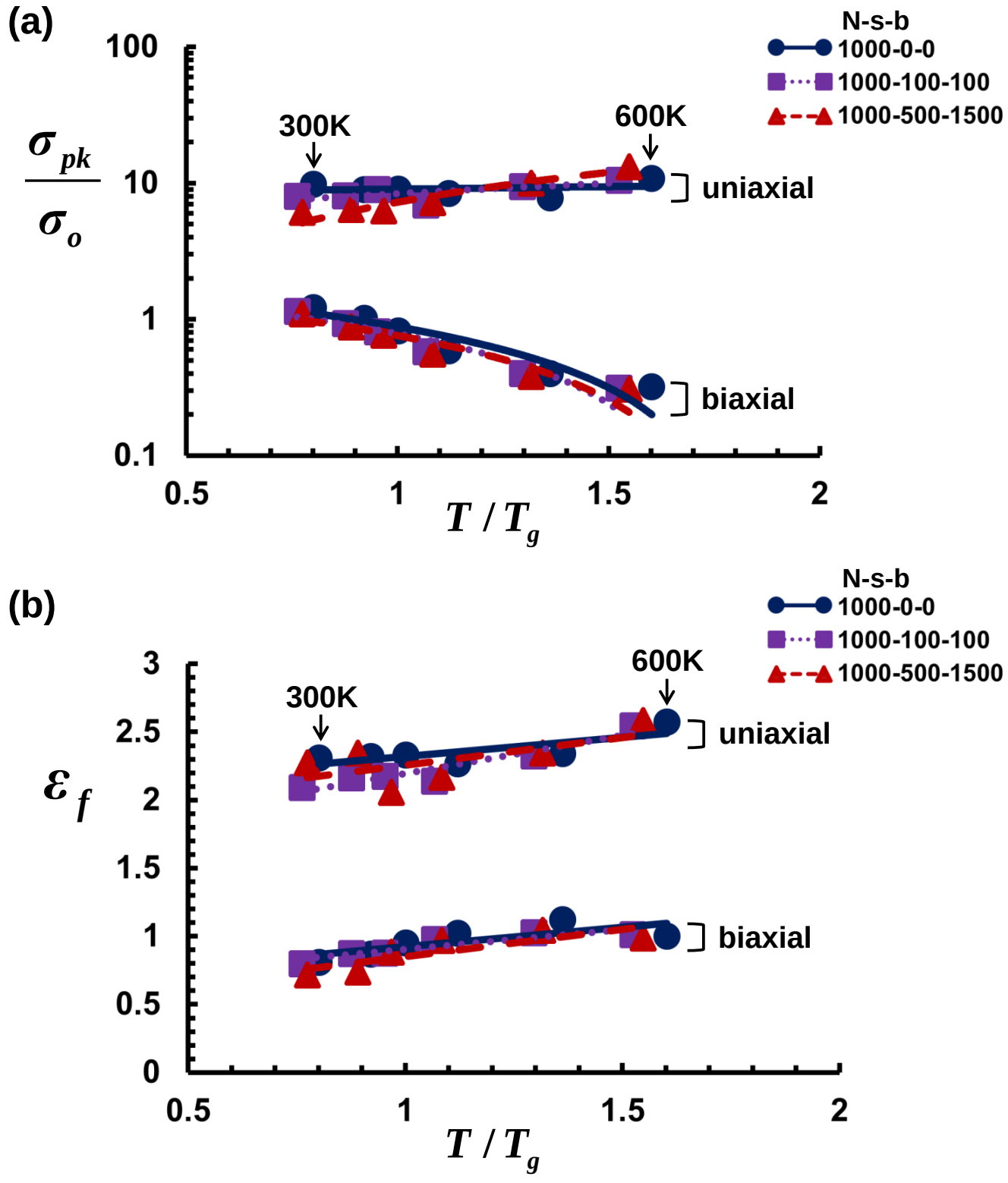

Figure 11: (a) Tensile peak stress σ_{pk}/σ_o versus T/T_g and (b) tensile failure strain ϵ_f versus T/T_g, for a thickness $h = 24$ nm and selected degrees of side-branching.

expansion [35].

A cell growth model has been developed by Van Loock et al. [35] to predict the expansion of equi-sized, spherical, gas-filled cells, as shown in Fig. S1, during solid-state nanofoaming of PMMA by CO_2. The thickness of the cell wall H_{cw}, as given by equation (S.12), is defined as the smallest distance of the solid ligament between two neighbouring cells. It is assumed that rupture of the cell wall occurs when the true hoop strain ϵ_s, as given by equation (S.11), at the inner surface of the cell equals the temperature-dependent, true tensile failure strain ϵ_f of the cell wall: $\epsilon_s = \epsilon_f$. The ductility-governed porosity limit f_f, as given by equation (S.17), then reads

$$f_f = \left\{ 1 + \exp\left(-3\epsilon_f\right) \left[\left(\frac{a_o}{0.5H_{cw} + a_o} \right)^{-3} - 1 \right] \right\}^{-1}, \tag{5}$$

where H_{cw}, as defined in equation (S.12), is the initial cell wall thickness, and a_o is the initial inner radius of the spherical cell, see Fig. S1a. Based on this ductility-governed porosity model, the microstructural transition from closed-celled to open-celled occurs when the porosity equals f_f.

We proceed to explore the sensitivity of nanofoam porosity to the cell wall failure strain ϵ_f by making use of equation (5) and the ductility data from the MD-predicted, equi-biaxial tensile response of PMMA films. Take the initial cell wall thickness H_{cw} to equal the film thickness h in the reference configuration: $H_{cw} = h$. This allows us to make use of the thickness-dependent, equi-biaxial tensile ductility ϵ_f of the linear (N-s-b: 1000-0-0) PMMA films, recall Fig. 7b, as an approximation for the tensile failure strain of the cell walls. The values of the cell wall thickness are $H_{cw} = 7.9$ nm, 24.5 nm, and 48.3 nm, thereby giving $H_{cw}/d_{ee} = 0.17$, 0.54, and 1.06, respectively. The ductility-governed porosity limit f_f, as stated by equation (5), is plotted in Fig. 12 as a function of foaming temperature T_f relative to T_g. Note that the initial inner radius a_o of the spherical cell is estimated to equal 10.5 nm for all cell wall thicknesses, as reported for the PMMA nanofoams of chain structure (N-s-b: 924-0-0) [35]. For reference, the measured values of final porosity are plotted in Fig. 12 for the PMMA nanofoams, of chain structure (N-s-b: 924-0-0), for a solid-state foaming period of 300 s [35]; the measured value of T_g for this PMMA grade equals 388 K [35].

Although approximations have been made in the model to simplify the cell wall geometry and the foaming conditions, the MD-predicted responses of porosity versus foaming temperature are in good agreement with the solid-state nanofoaming measurements, see Fig. 12. The measured final porosity f increases from $f = 0.51$ at $T_f/T_g = 0.77$ to $f = 0.75$, for the choice $T_f/T_g = 0.91$ in the glassy regime. At an increased foaming temperature of $T_f/T_g = 0.96$ close to the glass transition, f decreases to $f = 0.62$; this is due to collapse of the foamed microstructure, preceded by cell wall rupture [35]. Similar trends of f_f versus T_f/T_g are predicted for the explored range of cell wall of thickness. For example, for $H_{cw} = 48.3$ nm ($H_{cw}/d_{ee} = 1.06$), the predicted value of f_f increases from $f_f = 0.47$ at $T_f/T_g = 0.74$ to $f_f = 0.75$ at $T_f/T_g = 1.04$ just above the glass transition, then decreases to $f_f = 0.7$ at $T_f/T_g = 1.27$ followed by an almost plateau beyond this temperature. For thinner cell walls, the maximum values of f_f occur in the viscous regime: $f_f = 0.78$ at $T_f/T_g = 1.26$ for $H_{cw} = 7.9$ nm ($H_{cw}/d_{ee} = 0.17$), and $f_f = 0.76$ at $T_f/T_g = 1.36$ for $H_{cw} = 24.5$ nm ($H_{cw}/d_{ee} = 0.54$). Within the temperature regime typically used for solid-state nanofoaming of PMMA, i.e. $0.77 \leq T_f/T_g < 1$, the predicted porosity limit f_f exhibits a negligible sensitivity to cell wall thickness H_{cw}.

5. Concluding remarks

In the present study we have demonstrated the usefulness of MD simulations in quantitatively characterising the thickness-dependent tensile response of linear and side-branched PMMA films over a wide range of film thickness and temperature. The mass density profile through the thickness of a film is an indication of the enhanced molecular mobility near a free surface. The MD-predicted value of T_g for the film is depressed from the corresponding bulk value, and decreases with decreasing thickness, in qualitative agreement with the experimental observations for the free−standing PMMA films [13]. As the temperature increases from 300 K to 600 K (giving $0.76 \leq T/T_g \leq 1.79$), the characteristic transition from an elastic-plastic behaviour in the glassy regime through the glass transition regime to the viscous regime is captured, consistent with the observed behaviour for bulk PMMA of comparable molecular weight [35].

In order to gain insight into the molecular mechanisms by which ultrathin films fail in

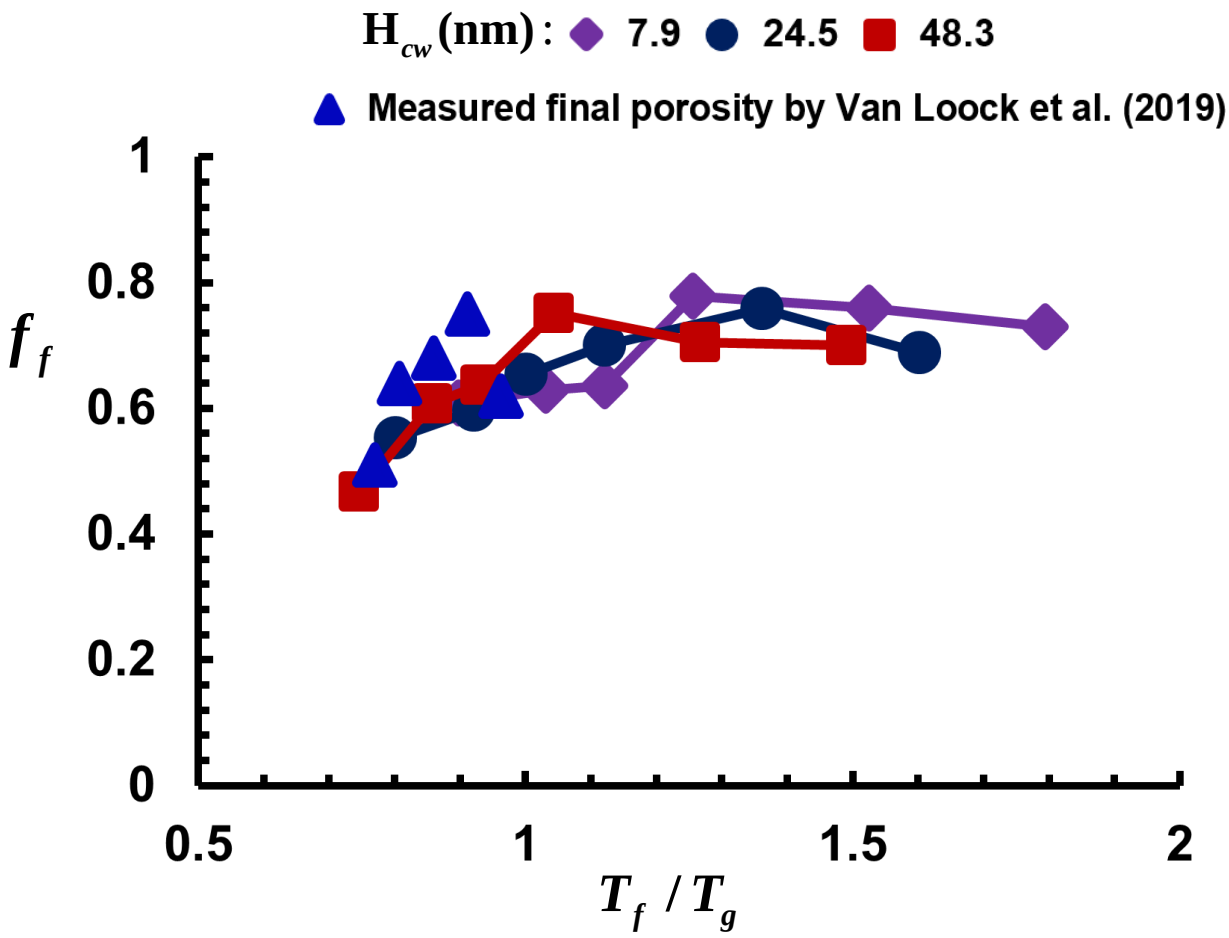

Figure 12: Porosity limit f_f versus T_f/T_g for the PMMA nanofoams of chain structure (N-s-b: 1000-0-0). The values of the cell wall thickness are H_{cw} = 7.9 nm, 24.5 nm, and 48.3 nm. For reference, the measured values of final porosity are included for PMMA nanofoams, of chain structure (N-s-b: 924-0-0), for a solid-state foaming period of 300 s [35].

tension, the tensile peak stress σ_{pk}/σ_o and the corresponding failure strain ϵ_f are identified, and plotted as functions of T/T_g and h/d_{ee} for selected molecular structures. The tensile failure strain ϵ_f decreases with decreasing temperature, with decreasing molecular weight, and with decreasing thickness for the uniaxial and equi-biaxial tensile straining, reflecting the combined effect of segmental mobility, chain confinement, and interchain entanglements. Within each temperature regime, the sensitivity of ϵ_f to the degree of side-branching is found to be minor. Furthermore, we have revealed that tensile failure is by the initiation and growth of voids at the free surfaces, followed by void expansion and propagation in the through-thickness direction. These results provide a molecular basis for understanding why the cell walls of PMMA nanofoams become susceptible to undesirable, early failure when their thickness is on the order of the end-to-end distance of the polymer molecules [35, 57].

In the present study, we have adopted a simple coarse-graining approach: each PMMA monomer is treated as one bead, and the polymer chains are considered as fully flexible bead-spring chains with zero intrinsic bending stiffness. It would be straightforward to increase the degree of complexity from different perspectives. For example, the current framework would allow us to (1) design molecular-level chemical and architectural features associated with the backbone, side-branches, and polymer networks; (2) model the significance of molecular architectural or structural defects in mechanical response; and (3) probe more sophisticated intrachain/interchain interactions and deformation characteristics.

Acknowledgements

The authors are grateful for the financial support from SABIC and the technical assistance from Dr. Martin van Es. We also acknowledge financial support from the ERC MULTILAT, grant number 669764. This work was performed using resources provided by the Cambridge Service for Data Driven Discovery (CSD3) operated by the University of Cambridge Research Computing Service (http://www.csd3.cam.ac.uk/), provided by Dell EMC and Intel using Tier-2 funding from the Engineering and Physical Sciences Research Council (capital grant EP/P020259/1), and DiRAC funding from the Science and Technology Facilities Council (www.dirac.ac.uk).

References

[1] P. G. de Gennes, *Scaling Concepts in Polymer Physics*. Cornell University Press, 1979.

[2] H. R. Brown and T. P. Russell, "Entanglements at polymer surfaces and interfaces," *Macromolecules*, vol. 29, no. 2, pp. 798–800, 1996.

[3] R. L. Jones, S. K. Kumar, D. L. Ho, R. M. Briber, and T. P. Russell, "Chain conformation in ultrathin polymer films," *Nature*, vol. 400, p. 146–149, 1999.

[4] J. M. Rathfon, R. W. Cohn, A. J. Crosby, J. P. Rothstein, and G. N. Tew, "Confinement effects on chain entanglement in free-standing polystyrene ultrathin films," *Macromolecules*, vol. 44, no. 13, pp. 5436–5442, 2011.

[5] L. Si, M. V. Massa, K. Dalnoki-Veress, H. R. Brown, and R. A. L. Jones, "Chain entanglement in thin freestanding polymer films," *Phys. Rev. Lett.*, vol. 94, p. 127801, 2005.

[6] M. D. Ediger and J. A. Forrest, "Dynamics near free surfaces and the glass transition in thin polymer films: A view to the future," *Macromolecules*, vol. 47, no. 2, pp. 471–478, 2014.

[7] J. L. Keddie, R. A. L. Jones, and R. A. Cory, "Size-dependent depression of the glass transition temperature in polymer films," *Europhysics Letters (EPL)*, vol. 27, no. 1, pp. 59–64, 1994.

[8] J. A. Forrest, K. Dalnoki-Veress, J. R. Stevens, and J. R. Dutcher, "Effect of free surfaces on the glass transition temperature of thin polymer films," *Phys. Rev. Lett.*, vol. 77, pp. 2002–2005, 1996.

[9] Y. Liu, Y. Chen, S. Hutchens, J. Lawrence, T. Emrick, and A. J. Crosby, "Directly measuring the complete stress–strain response of ultrathin polymer films," *Macromolecules*, vol. 48, no. 18, pp. 6534–6540, 2015.

[10] R. K. Bay, S. Shimomura, Y. Liu, M. Ilton, and A. J. Crosby, "Confinement effect on strain localizations in glassy polymer films," *Macromolecules*, vol. 51, no. 10, pp. 3647–3653, 2018.

[11] W. J. Choi, R. K. Bay, and A. J. Crosby, "Tensile properties of ultrathin bisphenol-A polycarbonate films," *Macromolecules*, vol. 52, no. 19, pp. 7489–7494, 2019.

[12] D. Liu, H. Qin, J. Zhang, and T. Wang, "Thickness-dependent glass transition temperature and charge mobility in cross-linked polyfluorene thin films," *Phys. Rev. E*, vol. 94, p. 052503, 2016.

[13] C. B. Roth, A. Pound, S. W. Kamp, C. A. Murray, and J. R. Dutcher, "Molecular-weight dependence of the glass transition temperature of freely-standing poly(methyl methacrylate) films," *The European Physical Journal E*, vol. 20, no. 4, pp. 441–448, 2006.

[14] O. A. Hasan, M. C. Boyce, X. S. Li, and S. Berko, "An investigation of the yield and postyield behavior and corresponding structure of poly(methyl methacrylate)," *Journal of Polymer Science.*, vol. 31, no. 2, pp. 185–197, 1993.

[15] Z. Li and J. Lambros, "Strain rate effects on the thermomechanical behavior of polymers," *International Journal of Solids and Structures*, vol. 38, no. 20, pp. 3549–3562, 2001.

[16] F. V. Loock and N. A. Fleck, "Deformation and failure maps for PMMA in uniaxial tension," *Polymer*, vol. 148, pp. 259–268, 2018.

[17] R. A. Duckett, S. Rabinowitz, and I. M. Ward, "The strain-rate, temperature and pressure dependence of yield of isotropic poly(methylmethacrylate) and poly(ethylene terephthalate)," *Journal of Materials Science*, vol. 5, no. 10, pp. 909–915, 1970.

[18] E. M. Arruda, M. C. Boyce, and R. Jayachandran, "Effects of strain rate, temperature and thermomechanical coupling on the finite strain deformation of glassy polymers," *Mechanics of Materials*, vol. 19, no. 2, pp. 193–212, 1995.

[19] P. Dooling, C. Buckley, S. Rostami, and N. Zahlan, "Hot-drawing of poly(methyl methacrylate) and simulation using a glass–rubber constitutive model," *Polymer*, vol. 43, no. 8, pp. 2451–2465, 2002.

[20] G. Palm, R. Dupaix, and J. Castro, "Large strain mechanical behavior of poly (methyl methacrylate) (PMMA) near the glass transition temperature," *Journal of Engineering Materials and Technology, Transactions of the ASME*, vol. 128, no. 4, pp. 559–563, 2006.

[21] J. Rottler and M. O. Robbins, "Growth, microstructure, and failure of crazes in glassy polymers," *Phys. Rev. E*, vol. 68, p. 011801, 2003.

[22] C. Chen, P. Depa, J. K. Maranas, and V. Garcia Sakai, "Comparison of explicit atom, united atom, and coarse-grained simulations of poly(methyl methacrylate)," *The Journal of Chemical Physics*, vol. 128, no. 12, p. 124906, 2008.

[23] P. Depa, C. Chen, and J. K. Maranas, "Why are coarse-grained force fields too fast? A look at dynamics of four coarse-grained polymers," *The Journal of Chemical Physics*, vol. 134, no. 1, p. 014903, 2011.

[24] R. G. Uttarwar, J. Potoff, and Y. Huang, "Study on interfacial interaction between polymer and nanoparticle in a nanocoating matrix: A martini coarse-graining method," *Industrial & Engineering Chemistry Research*, vol. 52, no. 1, pp. 73–82, 2013.

[25] K. Min, M. Silberstein, and N. R. Aluru, "Crosslinking PMMA: Molecular dynamics investigation of the shear response," *Journal of Polymer Science Part B: Polymer Physics*, vol. 52, no. 6, pp. 444–449, 2014.

[26] M. Mohammadi, H. fazli, M. karevan, and J. Davoodi, "The glass transition temperature of PMMA: A molecular dynamics study and comparison of various determination methods," *European Polymer Journal*, vol. 91, pp. 121–133, 2017.

[27] R. O. Dror, R. M. Dirks, J. P. Grossman, H. Xu, and D. E. Shaw, "Biomolecular simulation: A computational microscope for molecular biology," *Annual Review of Biophysics*, vol. 41, no. 1, pp. 429–452, 2012.

[28] L. Zhang, J. Jasa, G. Gazonas, A. Jérusalem, and M. Negahban, "Extracting continuum-like deformation and stress from molecular dynamics simulations," *Computer Methods in Applied Mechanics and Engineering*, vol. 283, no. 0, pp. 1010–1031, 2015.

[29] T. Mori, N. Miyashita, W. Im, M. Feig, and Y. Sugita, "Molecular dynamics simulations of biological membranes and membrane proteins using enhanced conformational sampling algorithms," *Biochimica et Biophysica Acta (BBA)-Biomembranes*, vol. 1858, no. 7, Part B, pp. 1635–1651, 2016.

[30] Z. Zhang, L. Zhang, J. Jasa, W. Li, G. Gazonas, and M. Negahban, "High fidelity computational characterization of the mechanical response of thermally aged polycarbonate," *Modelling and Simulation in Materials Science and Engineering*, vol. 25, no. 5, p. 055012, 2017.

[31] M. Tuckerman, *Statistical Mechanics: Theory and Molecular Simulation*. Oxford University Press, 2010.

[32] E. B. Tadmor and R. E. Miller, *Modeling Materials: Continuum, Atomistic and Multiscale Techniques*. Cambridge University Press, 2011.

[33] S. Plimpton, "Fast parallel algorithms for short-range molecular dynamics," *Journal of Computational Physics*, vol. 117, no. 1, pp. 1–19, 1995.

[34] W. Humphrey, A. Dalke, and K. Schulten, "VMD: visual molecular dynamics," *Journal of Molecular Graphics*, vol. 14, no. 1, pp. 33–38, 1996.

[35] F. Van Loock, V. Bernardo, M. A. Rodríguez Pérez, and N. A. Fleck, "The mechanics of solid-state nanofoaming," *Proceedings of the Royal Society A: Mathematical, Physical and Engineering Sciences*, vol. 475, no. 2230, p. 20190339, 2019.

[36] G. S. Grest and K. Kremer, "Molecular dynamics simulation for polymers in the presence of a heat bath," *Phys. Rev. A*, vol. 33, pp. 3628–3631, 1986.

[37] M. Bishop, M. H. Kalos, and H. L. Frisch, "Molecular dynamics of polymeric systems," *The Journal of Chemical Physics*, vol. 70, no. 3, pp. 1299–1304, 1979.

[38] M. Solar, H. Meyer, C. Gauthier, O. Benzerara, H. Pelletier, R. Schirrer, and J. Baschnagel, "Molecular dynamics simulations as a way to investigate the local physics of contact mechanics: a comparison between experimental data and numerical results," *Journal of Physics D: Applied Physics*, vol. 43, no. 45, p. 455406, 2010.

[39] B. Zhang, "Separation strain rate dependence on the failure of polymer adhesion with mobile promoters," *International Journal of Solids and Structures*, vol. 50, no. 25, pp. 4349 – 4354, 2013.

[40] H. R. Warner, "Kinetic theory and rheology of dilute suspensions of finitely extendible dumbbells," *Ind. Eng. Chem. Fundam.*, vol. 11, no. 3, pp. 379–387, 1972.

[41] B. P. Haley, N. Wilson, C. Li, A. Arguelles, E. Jaramillo, and A. Strachan, "Polymer Modeler, https://nanohub.org/resources/polymod," 2010.

[42] S. Peter, H. Meyer, and J. Baschnagel, "Thickness-dependent reduction of the glass-transition temperature in thin polymer films with a free surface," *Journal of Polymer Science Part B: Polymer Physics*, vol. 44, no. 20, pp. 2951–2967, 2006.

[43] J. A. Torres, P. F. Nealey, and J. J. de Pablo, "Molecular simulation of ultrathin polymeric films near the glass transition," *Phys. Rev. Lett.*, vol. 85, pp. 3221–3224, 2000.

[44] in *Theory of Simple Liquids With Applications to Soft Matter* (J.-P. Hansen and I. R. McDonald, eds.), Oxford: Academic Press, fourth edition ed., 2013.

[45] L. J. Fetters, D. J. Lohse, D. Richter, T. A. Witten, and A. Zirkel, "Connection between polymer molecular weight, density, chain dimensions, and melt viscoelastic properties," *Macromolecules*, vol. 27, no. 17, pp. 4639–4647, 1994.

[46] H. Aoki, S. Morita, R. Sekine, and S. Ito, "Conformation of single poly(methyl methacrylate) chains in an ultra-thin film studied by scanning near-field optical microscopy," *Polymer Journal*, vol. 40, p. 274–280, 2008.

[47] H. Aoki, K. Mori, T. Takahashi, and S. Ito, "Quantitative analysis of end-to-end distance of single polymer chain in ultra-thin film by super-resolution fluorescence imaging," *Chemical Physics*, vol. 419, pp. 54 – 58, 2013.

[48] J. M. Hutchinson, "Determination of the glass transition temperature," *Journal of Thermal Analysis and Calorimetry*, vol. 98, no. 3, p. 579, 2009.

[49] S. Napolitano, E. Glynos, and N. B. Tito, "Glass transition of polymers in bulk, confined geometries, and near interfaces," *Reports on Progress in Physics*, vol. 80, no. 3, p. 036602, 2017.

[50] J. A. Zimmerman, E. B. WebbIII, J. J. Hoyt, R. E. Jones, P. A. Klein, and D. J. Bammann, "Calculation of stress in atomistic simulation," *Modelling and Simulation in Materials Science and Engineering*, vol. 12, no. 4, p. S319, 2004.

[51] L. Zhang, Z. Zhang, J. Jasa, D. Li, R. O. Cleveland, M. Negahban, and A. Jérusalem, "Molecular dynamics simulations of heterogeneous cell membranes in response to uniaxial membrane stretches at high loading rates," *Scientific Reports*, vol. 7, no. 8316, 2017.

[52] L. Zhang, Z. Zhang, M. Negahban, and A. Jérusalem, "Molecular dynamics simulation of cell membrane pore sealing," *Extreme Mechanics Letters*, vol. 27, pp. 83–93, 2019.

[53] J. McLoughlin and A. Tobolsky, "The viscoelastic behavior of polymethyl methacrylate," *Journal of Colloid Science*, vol. 7, no. 6, pp. 555–568, 1952.

[54] S. Costeux, "CO_2-blown nanocellular foams," *Journal of Applied Polymer Science*, vol. 131, no. 23, 2014.

[55] J. Martín-de León, V. Bernardo, and M. A. Rodríguez-Pérez, "Key production parameters to obtain transparent nanocellular PMMA," *Macromolecular Materials and Engineering*, vol. 302, no. 12, p. 1700343, 2017.

[56] G. Wang, C. Wang, J. Zhao, G. Wang, C. B. Park, and G. Zhao, "Modelling of thermal transport through a nanocellular polymer foam: toward the generation of a new superinsulating material," *Nanoscale*, vol. 9, pp. 5996–6009, 2017.

[57] J. Pinto, B. Notario, R. Verdejo, M. Dumon, S. Costeux, and M. A. Rodriguez-Perez, "Molecular confinement of solid and gaseous phases of self-standing bulk nanoporous

polymers inducing enhanced and unexpected physical properties," *Polymer*, vol. 113, pp. 27–33, 2017.

Supplementary Information: Molecular dynamics simulations of ultrathin PMMA films

Lili Zhang[1] and Norman A. Fleck

Cambridge University, Engineering Department, Trumpington Street, Cambridge, CB2 1PZ, UK

Corresponding authors: lz399@cam.ac.uk (L. Zhang) and naf1@cam.ac.uk (N.A. Fleck)

Calculation of the film thickness

The film thickness h is determined by following the definition in Ref. [1] via the method of Gibbs dividing surface (GDS) [2]. First, the particle number density profile $\phi(r_3)$ in the 3−direction, see Fig. 2a, can be expressed as

$$\phi(r_3) = \frac{1}{A}\left[\sum_{i=1}^{n} \delta(r_3 - r_{i\_3})\right], \tag{S.1}$$

where, $A = l_1 l_2$ denotes the area of the simulation box parallel to the $1-2$ plane, r_{i_3} denotes the 3−component of $\mathbf{r}_i$ (the position vector of particle i), and n denotes the total number of particles in the box. The mean number density of the film, $\bar{\phi}$, is then calculated by averaging $\phi(r_3)$ over an interval of $\Delta = 1.5$ nm in the center r_{c_3} of the film

$$\bar{\phi} = \frac{1}{\Delta}\int_{r_{c\_3}-\Delta/2}^{r_{c\_3}+\Delta/2} \phi(r_3) dr_3. \tag{S.2}$$

The positions of the bottom GDS, r_-^G, and the top GDS, r_+^G, can be found, respectively, by

$$r_+^G = r_{c\_3} + \frac{1}{\bar{\phi}}\int_{r_{c\_3}}^{+\infty} \phi(r_3) dr_3, \tag{S.3}$$

and

$$r_-^G = r_{c\_3} - \frac{1}{\bar{\phi}}\int_{-\infty}^{r_{c\_3}} \phi(r_3) dr_3. \tag{S.4}$$

[1]Current affiliation: Aarhus University, Department of Mechanical and Production Engineering, Inge Lehmanns Gade 10, 8000 Aarhus C, Denmark

The film thickness h can be obtained via

$$h = r_+^G - r_-^G. \tag{S.5}$$

The value of h only weakly depends upon the value of Δ, consistent with the findings in Ref. [1], for the film systems in the present study.

Virial stress

Let a subscript index i, for example, identify the particle, so that m_i and $\mathbf{r}_i$ are the mass and position of particle i, respectively. Ω denotes the set of all indices for the selected particles. In this study, the set Ω comprises all PMMA chains in the system. As shown in Fig. 2b, both internal interaction forces, in the form of forces between the particles within Ω, and external interaction forces, as applied by particles outside Ω on particles inside Ω, are considered. Let $\mathbf{P}_i$ denote the resultant external force on particle i, where $\mathbf{P}_i$ includes any existing body forces and all forces between particles that reside inside and outside Ω. Let $\mathbf{f}_{ij}$ denote the internal force by particle j on particle i (where $i, j \in \Omega$). Then, by Newton's third law we have

$$\mathbf{f}_{ij} = -\mathbf{f}_{ji}. \tag{S.6}$$

The motion of particle i ($i \in \Omega$) is governed by Newton's second law such that

$$m_i \ddot{\mathbf{r}}_i = \sum_{j \in \Omega, j \neq i} \mathbf{f}_{ij} + \mathbf{P}_i. \tag{S.7}$$

A number of methods have been developed to interpret the discrete particle quantities obtained from the MD simulations in terms of the continuum measures of stress and strain. The most significant of these are (i) the virial stress for systems in thermodynamic equilibrium, and (ii) the Irving-Kirkwood-Noll procedure [3, 4], and its generalization by Hardy [5] for inhomogeneous and out-of-equilibrium systems, along with various extensions and adaptations [6, 7, 8, 9, 10, 11, 12, 13, 14, 15, 16, 17]. A multiscale framework has recently been proposed through which the continuum-like deformation gradient [18], Cauchy stress [18], and "interaction stress" [19] can be extracted for any arbitrary parts of an inhomogeneous MD system, in a manner that is consistent with classical continuum mechanics concepts.

The virial stress $\boldsymbol{\sigma}_t$ is based on the virial theorem of Clausius [20], and can be written as [6]

$$\boldsymbol{\sigma}_t = \frac{1}{V_t} \sum_{i \in \Omega} \left[\frac{1}{2} \sum_{j \in \Omega, j \neq i} (\mathbf{r}_j - \mathbf{r}_i) \otimes \mathbf{f}_{ij} - m_i \tilde{\mathbf{v}}_i \otimes \tilde{\mathbf{v}}_i \right], \tag{S.8}$$

where V_t is the volume of the total system, $\tilde{\mathbf{v}}_i$ is the thermal excitation velocity of particle i, and "$\otimes$" denotes the tensor product. This definition of virial stress comprises two terms: the potential part and the kinetic part involving the instantaneous velocities only due to thermal fluctuation.

Cell growth model and ductility-governed porosity limit

A cell growth model has recently been developed to predict the evolution of porosity as a function of foaming time and foaming temperature during solid-state nanofoaming of PMMA [21]. We briefly review the kinematics of this model as follows, see Ref. [21] for additional details.

Consider a polymer-gas solid with equi-sized spherical cells. A cross section of the undeformed (reference) configuration for the spherical cell, of initial inner radius a_o and initial outer radius z_o, is shown in Fig. S1a. Assume that the cell remains spherical during expansion and that the solid surrounding the cell is incompressible. The deformed (current) configuration for the spherical cell, of inner radius a and outer radius z is shown in Fig. S1b. A material point within the cell wall, initially at radius R, is displaced to a radius r, such that

$$r^3 - a^3 = R^3 - a_o^3, \tag{S.9}$$

by incompressibility. In spherical coordinates (r, θ, ϕ), the true (that is, logarithmic) value of hoop strain, $\epsilon_{\theta\theta}$, reads

$$\epsilon_{\theta\theta} = \ln(\frac{r}{R}), \tag{S.10}$$

where $\epsilon_{\phi\phi} = \epsilon_{\theta\theta}$ by symmetry. Let ϵ_s denote the true hoop strain at the inner surface of the cell as given by

$$\epsilon_s = \epsilon_{\theta\theta}(r = a) = \ln(\frac{a}{a_o}). \tag{S.11}$$

Define the initial cell wall thickness H_{cw} as the solid ligament between two neighbouring cells in the undeformed configuration, such that

$$H_{cw} = 2(z_o - a_o). \tag{S.12}$$

The initial (as-nucleated) porosity f_o is defined as

$$f_o = \left(\frac{a_o}{z_o}\right)^3, \tag{S.13}$$

and the current porosity f is defined in a similar manner as

$$f = \left(\frac{a}{z}\right)^3. \tag{S.14}$$

Incompressibility dictates that

$$z^3 - a^3 = z_o^3 - a_o^3. \tag{S.15}$$

Now make use of equations (S.12)-(S.15) to express the current porosity f as a function of the initial cell wall thickness H_{cw}, the initial inner radius a_o of the cell, and the true hoop strain ϵ_s at the inner surface of the cell in the form

$$f = \left\{1 + \exp\left(-3\epsilon_s\right)\left[\left(\frac{a_o}{0.5H_{cw} + a_o}\right)^{-3} - 1\right]\right\}^{-1}. \tag{S.16}$$

Assume that the cell wall fails when ϵ_s equals the temperature-dependent true tensile failure strain ϵ_f of the cell wall, $\epsilon_s = \epsilon_f$. Then, the porosity limit f_f corresponding to this failure criterion reads

$$f_f = \left\{1 + \exp\left(-3\epsilon_f\right)\left[\left(\frac{a_o}{0.5H_{cw} + a_o}\right)^{-3} - 1\right]\right\}^{-1}, \tag{S.17}$$

where the initial inner radius a_o of the cell is estimated to be close to 10.5 nm for PMMA nanofoams of chain structure (N-s-b: 924-0-0) [21].

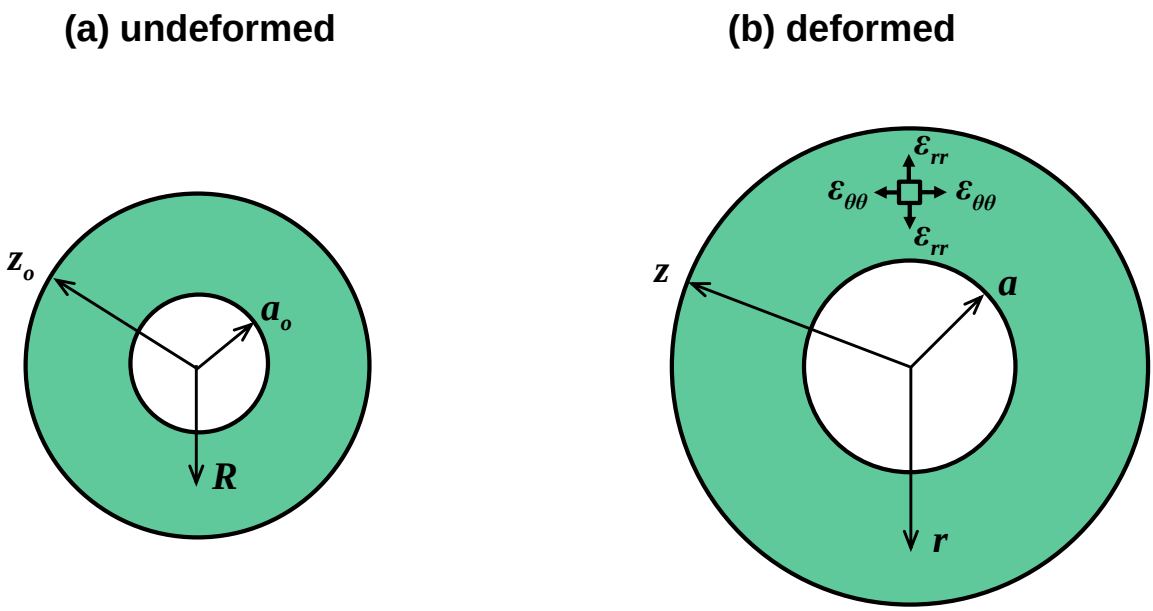

Figure S1: Spherical cell in (a) undeformed configuration with initial inner radius a_o and initial outer radius z_o and (b) deformed configuration with inner radius a and outer radius z.

Table 1. Equations of the best fitting straight lines in Figure 7

h (nm)	$\frac{\sigma_{pk}}{\sigma_o}$	ε_f
7.9	***Uni*:** $y = 4.64x + 0.12$	$y = 0.52x + 1.52$
	***Bi*:** $y = -0.60x + 1.31$	$y = 0.25x + 0.11$
24.5	***Uni*:** $y = 0.76x + 8.28$	$y = 0.28x + 2.04$
	***Bi*:** $y = -1.13x + 2.01$	$y = 0.28x + 0.64$
48.3	***Uni*:** $y = -0.60x + 12.45$	$y = 0.10x + 2.35$
	***Bi*:** $y = -1.81x + 3.03$	$y = 0.37x + 1.00$

References

[1] S. Peter, H. Meyer, and J. Baschnagel, "Thickness-dependent reduction of the glass-transition temperature in thin polymer films with a free surface," *Journal of Polymer Science Part B: Polymer Physics*, vol. 44, no. 20, pp. 2951–2967, 2006.

[2] in *Theory of Simple Liquids With Applications to Soft Matter* (J.-P. Hansen and I. R. McDonald, eds.), Oxford: Academic Press, fourth edition ed., 2013.

[3] J. H. Irving and J. G. Kirkwood, "The statistical mechanical theory of transport processes. IV. the equations of hydrodynamics," *The Journal of Chemical Physics*, vol. 18, no. 6, pp. 817–829, 1950.

[4] W. Noll, "Die herleitung der grundgleichungen der thermomechanik der kontinua aus der statistischen mechanik," *Indiana Univ. Math. J.*, vol. 4, no. 5, pp. 627–646, 1955.

[5] R. J. Hardy, "Formulas for determining local properties in molecular dynamics simulations: Shock waves," *The Journal of Chemical Physics*, vol. 76, no. 1, pp. 622–628, 1982.

[6] D. H. Tsai, "The virial theorem and stress calculation in molecular dynamics," *The Journal of Chemical Physics*, vol. 70, no. 3, pp. 1375–1382, 1979.

[7] K. S. Cheung and S. Yip, "Atomic-level stress in an inhomogeneous system," *Journal of Applied Physics*, vol. 70, no. 10, pp. 5688–5690, 1991.

[8] W. Chen and J. Fish, "A mathematical homogenization perspective of virial stress," *International Journal for Numerical Methods in Engineering*, vol. 67, no. 2, pp. 189–207, 2006.

[9] A. I. Murdoch, "A critique of atomistic definitions of the stress tensor," *Journal of Elasticity*, vol. 88, no. 2, pp. 113–140, 2007.

[10] J. A. Zimmerman, E. B. WebbIII, J. J. Hoyt, R. E. Jones, P. A. Klein, and D. J. Bammann, "Calculation of stress in atomistic simulation," *Modelling and Simulation in Materials Science and Engineering*, vol. 12, no. 4, p. S319, 2004.

[11] E. B. Webb, J. A. Zimmerman, and S. C. Seel, "Reconsideration of continuum thermomechanical quantities in atomic scale simulations," *Mathematics and Mechanics of Solids*, vol. 13, no. 3-4, pp. 221–266, 2008.

[12] J. A. Zimmerman, R. E. Jones, and J. A. Templeton, "A material frame approach for evaluating continuum variables in atomistic simulations," *Journal of Computational Physics*, vol. 229, no. 6, pp. 2364–2389, 2010.

[13] A. I. Murdoch, "On the identification of continuum concepts and fields with molecular variables," *Continuum Mechanics and Thermodynamics*, vol. 23, no. 1, pp. 1–26, 2011.

[14] J. Z. Yang, X. Wu, and X. Li, "A generalized Irving-Kirkwood formula for the calculation of stress in molecular dynamics models," *The Journal of Chemical Physics*, vol. 137, no. 13, p. 134104, 2012.

[15] D. Davydov and P. Steinmann, "Reviewing the roots of continuum formulations in molecular systems. Part III: Stresses, couple stresses, heat fluxes," *Mathematics and Mechanics of Solids*, vol. 20, no. 10, pp. 1153–1170, 2013.

[16] Y. Chen, "The origin of the distinction between microscopic formulas for stress and cauchy stress," *EPL (Europhysics Letters)*, vol. 116, no. 3, p. 34003, 2016.

[17] J. Rigelesaiyin, A. Diaz, W. Li, L. Xiong, and Y. Chen, "Asymmetry of the atomic-level stress tensor in homogeneous and inhomogeneous materials," *Proceedings of the Royal Society A: Mathematical, Physical and Engineering Sciences*, vol. 474, no. 2217, p. 20180155, 2018.

[18] L. Zhang, J. Jasa, G. Gazonas, A. Jérusalem, and M. Negahban, "Extracting continuum-like deformation and stress from molecular dynamics simulations," *Computer Methods in Applied Mechanics and Engineering*, vol. 283, no. 0, pp. 1010–1031, 2015.

[19] L. Zhang, Z. Zhang, J. Jasa, D. Li, R. O. Cleveland, M. Negahban, and A. Jérusalem, "Molecular dynamics simulations of heterogeneous cell membranes in response to uniaxial membrane stretches at high loading rates," *Scientific Reports*, vol. 7, no. 8316, 2017.

[20] R. Clausius, "Ueber einen auf die Wärme anwendbaren mechanischen Satz," *Poggendorffs Annalen*, vol. 141, pp. 124–130, 1870.

[21] F. Van Loock, V. Bernardo, M. A. Rodríguez Pérez, and N. A. Fleck, "The mechanics of solid-state nanofoaming," *Proceedings of the Royal Society A: Mathematical, Physical and Engineering Sciences*, vol. 475, no. 2230, p. 20190339, 2019.